scientific reports

OPEN

Radiation-induced synthesis of silver nanocomposites and their antibacterial applications

Wenbo Liu[1], Dominique Fourmy[2✉], Diana Dragoe[3], Hynd Remita[4✉] & Ruxandra Gref[1✉]

The global rise of antimicrobial resistance (AMR) poses a severe threat to public health, with multidrug-resistant pathogens undermining the efficacy of conventional antibiotics. Silver nanoparticles (AgNPs) have emerged as promising broad-spectrum antimicrobial agents. Here, we report a gamma radiation-assisted green synthesis of polyvinylpyrrolidone (PVP) or polyvinyl alcohol (PVA)-stabilized AgNPs, enabling rapid, sterile production of highly pure, uniformly dispersed nanoparticles without toxic byproducts, adapted for biomedical applications. Notably, AgNPs derived from Ag_2SO_4 precursor exhibited superior optical properties, and smaller homogeneous particle sizes compared to those from conventional $AgNO_3$. Optimized PVP-AgNPs demonstrated a well-known surface plasmon resonance near 396 nm, with sizes in the range of 5–25 nm as observed by transmission electron microscope, and a hydrodynamic diameter of ~ 33 nm. The physicochemical characterization of AgNPs was performed via different techniques such as X-ray photoelectron spectroscopy and powder X-ray diffraction. Importantly, PVP-/PVA-AgNPs displayed potent antibacterial activity, with minimum inhibitory concentrations of ~ 1 and 1–2 mg/L against *Staphylococcus aureus*, respectively, and 0.5 mg/L against *Pseudomonas aeruginosa* and *Escherichia coli*. These findings highlight the potential of green, radiation-synthesized AgNPs as a promising platform for next-generation antimicrobial materials in medical applications.

Antimicrobial therapy is increasingly challenged by the rise of antimicrobial resistance (AMR) and the emergence of novel infectious pathogens, posing a severe global public health crisis exacerbated by multidrug-resistant (MDR) infections and the rapid dissemination of resistant pathogens[1,2]. Among these, ESKAPE pathogens, including *Staphylococcus aureus* and *Pseudomonas aeruginosa*, have become dominant hospital-acquired infection agents, exhibiting heightened resistance to conventional antibiotics and significantly increasing treatment failure rates and mortality[1,3,4]. The widespread misuse and overuse of antibiotics remain primary drivers of bacterial resistance evolution. Indiscriminate antibiotic administration imposes selective pressure on bacterial populations, accelerating the evolution and dissemination of resistance genes. As such, the excessive use of β-lactam antibiotics has led to the rapid evolution of β-lactamases, enzymes capable of hydrolyzing the β-lactam ring and rendering these antibiotics ineffective[3,5]. Furthermore, bacteria utilize horizontal gene transfer mechanisms, like plasmids, transposons and integrons, to propagate resistance genes across different bacterial populations, contributing to the emergence of multidrug-resistant strains further[6]. These adaptive mechanisms have significantly reduced the clinical efficacy of traditional antibiotics, necessitating the development of novel antimicrobial agents with multi-target mechanisms to effectively combat resistant pathogens.

To mitigate the AMR crisis, researchers have focused on developing alternative antimicrobial strategies that complement or replace conventional antibiotics. A wide range of antimicrobial materials has been explored, including polymer-based antimicrobials like quaternary ammonium salts[7] and guanidine-functionalized polymers[8], photoactive antimicrobial materials like antimicrobial photodynamic therapy[9,10], biologically derived antimicrobial agents like antimicrobial peptides and lysozymes[11], carbon-based nanomaterials like graphene

[1]Institut de Sciences Moléculaires d'Orsay, UMR CNRS 8214, Université Paris-Saclay, Orsay 91400, France. [2]ENS Paris-Saclay, Laboratory of Biology and Applied Pharmacology (LBPA), CNRS UMR8113, Université Paris-Saclay, Gif-sur-Yvette 91190, France. [3]Institut de Chimie Moléculaire et des Matériaux d'Orsay, UMR 8182 CNRS, Université Paris-Saclay, Orsay 91405, France. [4]Institut de Chimie Physique, UMR 8000 CNRS, Université Paris-Saclay, Orsay 91405, France. ✉email: dominique.fourmy@ens-paris-saclay.fr; hynd.remita@universite-paris-saclay.fr; ruxandra.gref@cnrs.fr

oxide and carbon quantum dots[12,13]. Among these approaches, metal-based nanomaterials, particularly silver nanoparticles (AgNPs), have attracted significant attention due to their broad-spectrum antimicrobial activity and multiple bactericidal mechanisms, including cell membrane disruption reactive oxygen species generation, and DNA damage[14–16]. These multifaceted interactions significantly reduce the likelihood of bacterial resistance development, positioning AgNPs as a promising solution for combating MDR pathogens.

Silver has long been recognized for its antimicrobial properties, with historical applications dating back to ancient civilizations where silver vessels were used to preserve food and water[17]. The advancement of nanotechnology has further revolutionized Ag-based antimicrobial materials, expanding their applications like coatings, wound dressings, and drug delivery systems[18,19]. However, the antimicrobial efficacy of AgNPs is highly dependent on factors like synthesis method, particle size, and the choice of stabilizing agents. Traditional chemical reduction methods, which rely on reducing agents like sodium borohydride ($NaBH_4$) or hydrazine, often generate toxic byproducts that limit the biocompatibility of the resulting nanoparticles[20]. While biogenic synthesis offers an eco-friendly alternative, challenges like low yield, poor size control, and batch-to-batch variability hinder their scalability for biomedical applications[21]. Therefore, there is a critical need to develop a green, controllable, and scalable synthesis approach for AgNPs-based materials to ensure their practical implementation in medical applications.

Ionizing radiation-assisted in-situ reduction synthesis, particularly gamma radiation process, has emerged as a promising method for fabricating metal nanoparticles due to its unique advantages as compared to conventional chemical reduction methods[22,23]. In deoxygenated aqueous media, gamma irradiation generates highly reducing hydrated electrons which efficiently reduce silver ions (Ag^+) to elemental silver (Ag^0), leading to the formation of well-dispersed AgNPs with uniform size distribution[22,24–26]. Precise control over nanoparticle size and morphology is achieved by adjusting dose rate and the irradiation conditions[23]. Furthermore, radiation-assisted synthesis method avoids the need of toxic reducing agents such as $NaBH_4$ and hydrazine as the reducing species (solvated electrons and reducing radicals are induced by solvent radiolysis), thereby minimizing hazardous byproducts. More importantly, gamma radiation enables the direct synthesis of AgNP composites in aqueous and complex media, facilitating the production of biocompatible and/or biodegradable materials without the need for post-synthesis sterilization[18,23]. These advantages make radiation-synthesized AgNPs particularly suitable for biomedical applications, including antimicrobial coatings and wound dressings[27,28].

In radiation-assisted synthesis of AgNPs, the choice of silver precursors like silver nitrate ($AgNO_3$), silver sulfate (Ag_2SO_4), and silver perchlorate ($AgClO_4$), as well as the selection of stabilizing agents like polyvinylpyrrolidone (PVP), poly(3,4-ethylenedioxythiophene), chitosan, calixarenes, gelatin, carboxymethyl cellulose and polyvinyl alcohol (PVA), significantly influence the physicochemical properties and biological performance of the resulting AgNPs[29–32]. As reported previously, sulfate ions (SO_4^{2-}) form Ag–SO_4 complexes that modulate the reduction rate, leading to smaller and more uniformly distributed AgNPs, in contrast to widely used nitrate-based Ag precursors[33,34]. Furthermore, stabilizing agents like PVP not only improve AgNPs dispersion, but also enhance their biocompatibility, making them more suitable for antimicrobial applications[35,36]. Despite these advancements, systematic studies evaluating the influence of different silver precursors and stabilizers on the antimicrobial efficacy of radiation-synthesized AgNPs remain limited. In particular, research on their long-term stability and antimicrobial performance in complex biological environments is still lacking, highlighting a critical gap in the current literature.

To address these challenges, in this study gamma radiation-assisted synthesis is used to fabricate biocompatible AgNPs stabilized by PVP or PVA in aqueous media. It systematically investigates the effects of different silver precursors (Ag_2SO_4, $AgNO_3$, $AgClO_4$), PVP concentration, and radiation dose on nanoparticle size, dispersion, and antimicrobial efficacy. Additionally, the study evaluates the long-term stability of AgNPs under different storage conditions (4 °C, 25 °C, 37 °C) and assesses their antibacterial effects against both Gram-positive (*Staphylococcus aureus*) and Gram-negative bacteria (*Pseudomonas aeruginosa*, *Escherichia coli*). By addressing these critical factors, this study aims to provide a theoretical foundation and technical framework for the development of high-efficiency, stable, and environmentally friendly AgNP-based antimicrobial materials, produced by green gamma radiation-assisted in situ synthesis contributing to the global effort to combat antibiotic resistance.

Methods and materials
Materials
All chemicals were reagent-grade and used without further purification. Silver salts ($AgNO_3$, $AgClO_4$, Ag_2SO_4), isopropyl alcohol (IPA), PVA (30–70 kDa, 87–90% hydrolyzed), and PVP (40 kDa) were sourced from Sigma Aldrich (Saint Quentin Fallavier, France). *Staphylococcus aureus* ATCC 27217 (*S. aureus* ATCC 27217) bacteria strain was obtained from the American Type Culture Collection (ATCC). *Pseudomonas aeruginosa* PA14 (*P. aeruginosa* PA14)[37] and *Escherichia coli* MG1655 (*E. coli* MG1655) and *S. aureus* were all grown in cation-adjusted Mueller-Hinton-II broth (MHB-CA) (Becton, Dickinson and Company, USA) or Luria Bertani Broth (Sigma-Aldrich). Ultrapure water (Millipore) was used as the solvent, and argon gas for degassing was obtained from Air Liquide (France).

Radiolytic synthesis of PVP-stabilized AgNPs
The radiation-induced reduction synthesis of PVP-stabilized AgNPs (PVP-AgNPs) was conducted as follows: A well-dispersed aqueous solution (10 mL) containing a silver salt precursor (1 mM Ag^+) was prepared using $AgNO_3$, $AgClO_4$, or Ag_2SO_4, along with PVP (100 mM, monomer concentration) and isopropyl alcohol (100 mM). The solution was deoxygenated with argon gas for ~20 min. The synthesis was carried out using a panoramic γ-irradiation source from a ^{60}Co γ-facility (maximum dose rate of 1.8 kGy·h^{-1}) at the Institut de Chimie Physique, Orsay, France. All glassware used for handling the silver stock solution was soaked in fresh aqua regia (3:1 v/v

HCl/HNO3) overnight and thoroughly rinsed with ultrapure water. The physicochemical properties of the PVP-stabilized AgNPs were optimized by varying the reaction parameters like the concentration and type of silver precursor, concentration of PVP and total radiation dose. Additionally, PVA-stabilized AgNPs (PVA-AgNPs) were synthesized via radiation-assisted reduction methods, following our previous report[18]. In this case, Ag_2SO_4 (2 mM) and PVA (100 mM) were used instead of Ag_2SO_4 (1 mM) and PVP (60 mM) under the same irradiation conditions. After synthesis, both PVA-AgNPs and PVA-AgNPs were purged with nitrogen to remove dissolved gases and stored at 4 °C for future use.

Characterization of AgNPs

The ultraviolet-visible (UV-Vis) absorption spectra were recorded using a Varian Cary 300 UV-Vis spectrophotometer (Agilent) in the scanning range of 200 to 800 nm, with a 1.0 cm optical path length in a quartz cuvette. Ultrapure water was used as a reference unless otherwise specified.

Powder X-ray diffraction (PXRD) was performed to analyze the crystal phase of AgNPs at the MORPHEUS platform, Laboratoire de Physique des Solides, using an X-ray rotating anode generator (Rigaku Corp.) equipped with multilayer optics (Xenocs SA), delivering a monochromatic X-ray beam with a wavelength of λ(Cu Kα) = 1.541 Å. The AgNPs were purified and concentrated using the Vivaspin tubes with a 100 kDa cutoff (Vivaspin® 500 PES), then loaded into 1 mm borosilicate capillaries and flame-sealed. The average crystalline size of the AgNPs was calculated using the Scherrer equation (Eq. 1)[38]:

$$D = \frac{K\lambda}{\beta \cdot \cos\theta} \tag{1}$$

where D is the mean size of the ordered (crystalline) domains (in nm), K is the Scherrer constant (typically 0.9), λ is the X-ray wavelength (for Cu Kα radiation, 1.541 Å), β is the full width at half maximum (FWHM, in radians) of the peak, and θ is the diffraction (Bragg) angle in radians.

The morphologies of AgNPs were observed using a transmission electron microscope (TEM, JEOL 1400, Japan). The pristine AgNPs were deposited onto a carbon film-supported copper grid and analyzed at an acceleration voltage of 120 kV. The corresponding particle size and size distribution were measured using ImageJ (version 1.54d).

The hydrodynamic diameter (Z-average, nm) was measured using dynamic light scattering (DLS) with a Zetasizer Nano ZS (Malvern Instruments, UK) at a scattering angle of 90°. All particle size measurements were conducted at 25 °C in manual mode, with three independent readings taken in a disposable polystyrene cell.

Attenuated total reflectance Fourier transform infrared (ATR-FTIR) spectroscopy was used to analyze the chemical composition of both AgNP samples within the spectral range of 4000–500 cm^{-1} using a PerkinElmer® Spectrum Two FT-IR spectrometer equipped with a LiTaO$_3$ detector.

X-ray photoelectron spectroscopy (XPS) measurements were performed on a K-Alpha spectrometer from ThermoFisher, equipped with a monochromated X-ray Source (Al Kα, 1486.6 eV). A spot size of 400 μm was employed corresponding to an irradiated zone of ~ 1 mm^2. The hemispherical analyzer was operated in CAE (Constant Analyzer Energy) mode, with a pass energy of 200 eV, a step of 1 eV for the acquisition of surveys spectrum and a pass energy of 50 eV and a step of 0.1 eV for the acquisition of narrow scan spectra. A "dual beam" flood gun was used to neutralize the charge build-up. AgNP films were prepared on fluorine-doped oxide (FTO) glass and stored in a vacuum prior to the measurement, enabling high-resolution surface characterization. Spectral processing was performed using Avantage software with a peak-fitting routine incorporating Linear background subtraction and symmetrical 30% mixed Gaussian-Lorentzian line shapes. Atomic percentages were calculated through normalization of peak areas using Scofield sensitivity factors. The binding energy scale was calibrated against neutral carbon at 285 eV, with a precision of ± 0.2 eV.

Colloidal stability of AgNPs

The short-term (12 h) and long-term (1 month) colloidal stabilities of the AgNPs were evaluated under three storage conditions: 4 °C, 25 °C (room temperature), and 37 °C while keeping the samples under static conditions. The optimized AgNPs, appropriately diluted (10-fold for PVP-AgNP and 20-fold for PVA-AgNP), were stored in amber glass vials in the darkness. At different time intervals, three representative batches were withdrawn and analyzed by UV-Vis and DLS to monitor their physicochemical properties.

Bacterial strains culture

The Gram-positive bacterial strain *S. aureus* ATCC 27217 and the Gram-negative bacterial strains *P. aeruginosa* PA14 and *E. coli* MG1655 were streaked onto a Luria-Bertani agar (LBA) plate for cultivation. A bacterial culture was obtained by isolating a few single colonies and suspending them in 3 mL of sterile MHB-CA, followed by overnight incubation (16–18 h) at 180 RPM and 37 °C in a shaking incubator. The overnight bacterial culture was diluted in sterile MHB-CA for preculturing to obtain bacteria in the exponential growth phase. The optical density (OD$_{600}$) of bacteria in the growth phase was measured at 600 nm, where OD$_{600}$ of 1.0 corresponds to 8×10^8 colony-forming units (CFU)/mL. The standardized inoculum was further diluted as needed.

In vitro antibacterial evaluation of AgNPs

The minimum inhibitory concentrations (MIC) of both AgNPs were determined using a modified microdilution method, following the International Standard ISO 20776-1 recommended by EUCAST[39]. Briefly, the standardized inoculum was further diluted to 1×10^6 CFU/mL. Aliquots of each bacterial strain culture were mixed with 50 μL of MHA-CA-diluted AgNPs containing two-fold serial dilutions in a 96-well flat-bottomed microtiter plate in technical triplicate. Additionally, the undiluted filtrates from each AgNPs suspension mixed with the same final

bacterial density and the bacterial strain cultures with equivalent final density served as positive controls, while MHB-CA alone was the negative control. The AgNPs suspension filtrates were centrifuged at 50 RPM for 1 h and separated using the Vivaspin tubes with a 100 kDa of cut-off. The inoculated microtiter plate was incubated at 37 °C in an incubator overnight (16–18 h) with no shaking. The final OD_{600} of overnight bacterial culture was measured at 600 nm using a PerkinElmer® Victor X5 microplate reader. The MIC is defined as the lowest AgNPs concentration at which no visible bacterial growth is observed. Here, MIC is calculated as the lowest concentration of AgNPs at which no significant increase in OD_{600} is observed, indicating inhibition of bacterial growth. To determine the minimum bactericidal concentration (MBC), wells showing no visible bacterial growth in the MIC assay were selected, and the bacterial suspensions from these wells were diluted in sterile MHB-CA and dropped onto LBA plates. The MBC is defined as the lowest concentration of the antimicrobial agent that causes at least a 3 $\log^{10}$ reduction in the number of surviving cells after incubation, compared to the initial concentration[40].

SEM observation of bacterial morphology
The morphological changes of bacterial cells in the treatment of PVA-/PVP-AgNPs were examined by scanning electron microscopy (SEM) to evaluate surface attachment, membrane disruption, and potential intracellular localization. *S. aureus* ATCC 27217 and *P. aeruginosa* PA14 were cultured in the medium of MHB-CA and then standardized to 1×10^6 CFU/mL. Subsequently, the bacterial suspensions were exposed to both AgNPs at their respective MICs overnight at 37 °C. For each assay, aliquots of bacterial cells were dispensed into a 96-well microtiter plate, followed by the addition of 200 µL of PVA-/PVP-AgNPs. The mixtures were incubated at 37 °C for 18 h to allow sufficient interaction. After incubation, the samples were centrifuged at 6000 rpm for 5 min, the supernatant was discarded, and the pellets were washed twice with phosphate-buffered saline (PBS) to remove unbound AgNPs.

For SEM sample preparation, pellets were resuspended in 2.5% glutaraldehyde prepared in 0.1 M sodium cacodylate buffer (pH 7.2) and fixed overnight at 4 °C. Post-fixation, the cells were centrifuged at 6000 rpm for 5 min, the supernatant was removed, and the pellets were washed twice with PBS. Dehydration was performed by passing the samples sequentially through graded ethanol concentrations (30%, 50%, 70%, 80%, 90%, and 100%), followed by drying with hexamethyldisilazane. The dried specimens were mounted on silicon wafer substrates and sputter-coated with gold for SEM imaging. Imaging was conducted with a Zeiss 1540 SEM with an accelerating voltage of 1.5–3 kV to obtain high-resolution images.

Statistical analysis
All data were obtained from three independent experiments performed on different days, and data analysis was then performed using OriginPro 2021. All results were expressed as mean ± error bars (expressed in standard deviation (SD)) from triplicate independent samples unless otherwise specified.
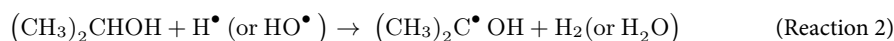
Results and discussion
Polyvinylpyrrolidone (PVP) was reported to stabilize AgNPs nanoparticles during their synthesis by various routes, allowing control over their sizes[35,36]. Although non-biodegradable, PVP is a water-soluble biocompatible polymer with low toxicity widely used for fabricating antibacterial medical materials[41,42]. This study investigates the influence of PVP (40 kDa) on the physicochemical properties of PVP-stabilized AgNP nanocomposites prepared by radiolysis, a convenient method allowing to obtain directly sterile medical materials. The PVP-AgNPs and PVA-AgNPs were characterized by TEM, UV-Vis spectroscopy, XPRD, XPS, and DLS particle size analysis. Among them, PVA-AgNPs were resynthesized with a maximum dose rate of 1.8 kGy·h^{-1}, referring to our previously reported protocol[18]. Compared to the previously synthesized ones (20.0 ± 2.0 nm) at 4.25 kGy·h^{-1}, the resynthesized PVA-AgNPs still displayed well-dispersed and uniformly spherical particles with a size distribution of 34.3 ± 4.7 nm, which confirmed by TEM images (Fig. S1). This change in size is attributed to the decay of ^{60}Co γ-radiation source dose rate with time[18].

Radiation-induced reduction mechanism in AgNP synthesis
The interaction of high-energy radiation (gamma rays, X-rays, electron beams, ion beams) with a polar solvent leads to its excitation and production of various radiolytic species, in case of water[43]:
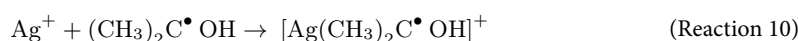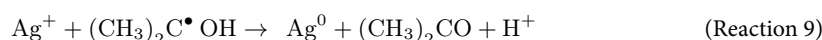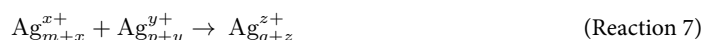
$$H_2O \rightarrow e_{aq}^-, HO^\bullet, H^\bullet, H_3O^+, H_2O_2, H_2, HO_2^{\cdot} \qquad \text{(Reaction 1)}$$
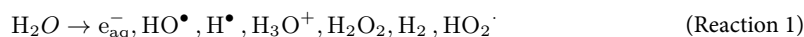
The radiolytic yield (*G*-value, expressed in mol·J^{-1}) represents the amount of radiolytic species formed per Joule of absorbed energy in the system[29]. Hydrated electrons e_{aq}^-, H• and hydroxyl radicals (HO•) are the most abundant and reactive transient species in the diluted aqueous solutions. e_{aq}^- is a strongly reducing highly reactive species with a redox potential of − 2.8 $V_{vs.\ SHE}$[24,44], H• is a reducing radical with a redox potential of − 2.3 $V_{vs.\ SHE}$[25], whereas HO• is a strongly oxidizing radical with a redox potential of $E°$ (HO•/H$_2$O) = 2.73 $V_{vs.\ SHE}$ at neutral pH[24,45]. Scavenging oxidizing species is essential for the γ-radiation-assisted reduction of silver ions. In this study, isopropyl alcohol was used as a scavenger for HO• and H• radicals. In the presence of a high concentration (100 mM) of isopropanol, both radicals are quantitatively scavenged to produce isopropanol radical $(CH_3)_2C•OH$ with reducing capacity (Reaction 2):

$$\left(CH_3\right)_2 CHOH + H^\bullet \ (or\ HO^\bullet) \rightarrow \left(CH_3\right)_2 C^\bullet OH + H_2(or\ H_2O) \qquad \text{(Reaction 2)}$$

γ-irradiation of deoxygenated, diluted Ag$^+$-containing aqueous solutions generates in the presence of (CH$_3$)$_2$CHOH two highly reactive transient species: e$_{aq}^-$ ($G = 2.8 \times 10^{-7}$ mol·J^{-1}) and (CH$_3$)$_2$C•OH ($G = 3.4 \times 10^{-7}$ mol·J^{-1}). Notably, (CH$_3$)$_2$C•OH acts as a reducing agent with a redox potential of -1.8 V$_{vs. SHE}$ at neutral pH [24,29].

Upon γ-irradiation, Ag$^+$ in the deoxygenated diluted aqueous solution is quantitatively reduced by (CH$_3$)$_2$C•OH and e$_{aq}^-$, forming silver atoms that further aggregate into Ag clusters or nanoscale silver species (Eqs. 2, 3, and 4). The reduction reaction process leading to AgNP formation is detailed in the reactions (3)–(9), as previously described[18,22,46]. Specifically, e$_{aq}^-$ produced by the radiolysis of water is highly reducing and can efficiently convert Ag$^+$ in solution to their elemental form. In addition, it is worth noting that the reduction of silver ions can also occur through the formation of a complex in which the metal ion is coordinated by an alcohol radical, serving as a ligand (reactions 10 and 11)[22,33].

$$Ag^+ + e_{aq}^- \rightarrow Ag^0 \qquad\qquad \text{(Reaction 3)}$$

$$Ag^0 + Ag^0 \rightarrow Ag_2 \qquad\qquad \text{(Reaction 4)}$$

$$Ag^0 + Ag^+ \rightarrow Ag_2^+ \qquad\qquad \text{(Reaction 5)}$$

$$Ag_n + Ag^+ \rightarrow Ag_{n+1}^+ \qquad\qquad \text{(Reaction 6)}$$

$$Ag_{m+x}^{x+} + Ag_{p+y}^{y+} \rightarrow Ag_{q+z}^{z+} \qquad\qquad \text{(Reaction 7)}$$

$$Ag_{n+1}^+ + e_{aq}^- \rightarrow Ag_{n+1} \qquad\qquad \text{(Reaction 8)}$$

$$Ag^+ + (CH_3)_2C^\bullet OH \rightarrow Ag^0 + (CH_3)_2CO + H^+ \qquad\qquad \text{(Reaction 9)}$$

$$Ag^+ + (CH_3)_2C^\bullet OH \rightarrow [Ag(CH_3)_2C^\bullet OH]^+ \qquad\qquad \text{(Reaction 10)}$$

$$[Ag(CH_3)_2COH]^+ + Ag^+ \rightarrow Ag_2^+ + (CH_3)_2CO + H^+ \qquad\qquad \text{(Reaction 11)}$$

In this study, PVP serves as a surface stabilizer and dispersant. When reacting with reducing species such as e$_{aq}^-$, PVP might undergo intramolecular or intermolecular cross-linking thus forming a multidimensional polymer network, which prevents the aggregation of AgNP by lowering the surface tension (Reaction 12)[47].

$$PVP + e_{aq}^- \rightarrow PVP^\bullet \rightarrow PVP - PVP \text{ (Crosslinked polymer)} \qquad\qquad \text{(Reaction 12)}$$
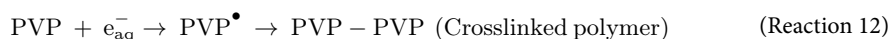
The irradiation dose D (measured in Grays, where 1 Gy = 1 J/kg or 1 J/L for a diluted solution), required for the quantitative consumption of a species in the irradiated aqueous medium, depends on the species' concentration (C) and the radiolytic yield (G). This relationship is expressed as follows:

$$D\,(\text{Gy}) = C\left(\text{mol} \cdot \text{L}^{-1}\right) / G\left(\text{mol} \cdot \text{J}^{-1}\right) \qquad\qquad (2)$$

All Ag$^+$ ions at 0.5 mM are theoretically reduced under deoxygenated aqueous conditions, enabling the quantitative synthesis of AgNPs at a total radiation dose of 1.0 kGy in the presence of isopropanol (Eq. 2).

Influence of silver precursors on AgNP growth

The irradiated silver solutions are brown and the UV-Vis spectra of diluted PVP-AgNP aqueous suspensions obtained with different silver salt precursors (Ag$_2$SO$_4$, AgNO$_3$, and AgClO$_4$) were recorded (Fig. 1). The AgNPs exhibited significant variations in both the position (λ_{SPR}) and intensity of the absorption peaks corresponding to surface plasmon resonance (SPR). The absorption peaks, observed at around 400 nm for all prepared AgNPs, correspond to the well-dispersed orange-colored sample solutions shown in the inset. These peaks are characteristic of the SPR of AgNPs (Fig. 1)[48,49].

As shown in Table 1, PVP-AgNP synthesized from Ag$_2$SO$_4$ (denoted as PVP-AgNP$_{Ag2SO4}$) exhibited the strongest absorption peak at 399.3 ± 2.2 nm with an absorbance of 0.72 ± 0.10, measured at the same initial silver ion concentration across all silver precursors (Ag$_2$SO$_4$, AgNO$_3$, and AgClO$_4$) used in this experiment. The presence of a single absorption peak in the UV-Vis spectrum suggests a homogeneous size distribution and small particle size, as confirmed by TEM (Fig. 2). In the TEM images, spherical PVP-AgNP$_{Ag2SO4}$ particles ranged from 5 to 20 nm in size, with a mean diameter of 45 ± 4 nm. Additionally, the lower full width at half maximum (FWHM) and polydispersity index (PDI) of PVP-AgNP$_{Ag2SO4}$ indicate better dispersibility compared to PVP-AgNP$_{AgNO3}$ and PVP-AgNP$_{AgClO4}$. Moreover, both PVP-AgNP$_{AgNO3}$ and PVP-AgNP$_{AgClO4}$ exhibited secondary absorption peaks in the range of 500–600 nm in the UV-Vis spectrum, indicating two distinct particle size distributions. Both PVP-AgNP$_{AgNO3}$ and PVP-AgNP$_{AgClO4}$ contain large particles (40–60 nm), as indicated by their high PDI of 0.53 ± 0.05 and 0.57 ± 0.09, respectively (Figs. 1 and 2, and Table 1).

Thus, in radiation-induced AgNP synthesis, the type of silver salt precursor significantly affects both the mean particle size and the particle size distribution. Meanwhile, previous pulse radiolysis studies using Ag$_2$SO$_4$ and AgClO$_4$ salts have demonstrated that sulfate ions (SO$_4^{2-}$) facilitate the disappearance of Ag$_2$ by forming complexes with Ag$_3^+$, promoting aggregation and leading to the formation of larger silver clusters or colloidal silver, compared to perchlorate ions (ClO$_4^-$)[33,34]. Therefore, sulfate ions play a significant role in regulating the growth kinetics and size distribution of AgNPs. More importantly, SO$_4^{2-}$ and ClO$_4^-$ do not react with radiolytically generated species, unlike nitrate ions[18]. The AgNP samples obtained from AgNO$_3$ precursor showed broad size distribution, which may be due to differences in the reduction rate induced by the consumption
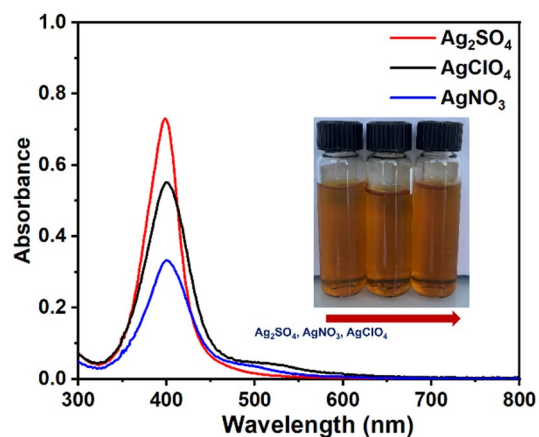
Fig. 1. Ultraviolet-visible absorption spectra of a γ-irradiated AgNP aqueous suspension diluted 10-fold in ultrapure water, showing the effects of different silver precursors at the silver ionic concentration of 1 mM: Ag_2SO_4, $AgNO_3$, and $AgClO_4$. Optical path length is 1.0 cm. Inset: Corresponding optical images of pristine PVP-AgNP samples.

Silver precursor	Absorbance ($\pm$ SD)	λ_{SPR} (nm) ($\pm$ SD)	FWHM (nm) ($\pm$ SD)	DLS size (nm) ($\pm$ SD)	PDI ($\pm$ SD)
Ag_2SO_4	0.72 ± 0.10	399.3 ± 2.2	51.5 ± 5.6	45.2 ± 4.6	0.47 ± 0.05
$AgNO_3$	0.36 ± 0.04	403.3 ± 2.6	56.0 ± 4.2	34.6 ± 8.8	0.53 ± 0.05
$AgClO_4$	0.54 ± 0.01	401.3 ± 1.5	54.7 ± 5.8	58.5 ± 12.7	0.57 ± 0.09

Table 1. Comparison of absorbances and absorption peaks (λ_{SPR}, nm) corresponding to the surface plasmon resonance, full width at half maximum (FWHM, nm), DLS particle size (nm), and polydispersity index (PDI) of PVP-AgNPs (10-fold diluted in ultrapure water) synthesized using different silver precursors (Ag_2SO_4, $AgNO_3$, and $AgClO_4$).
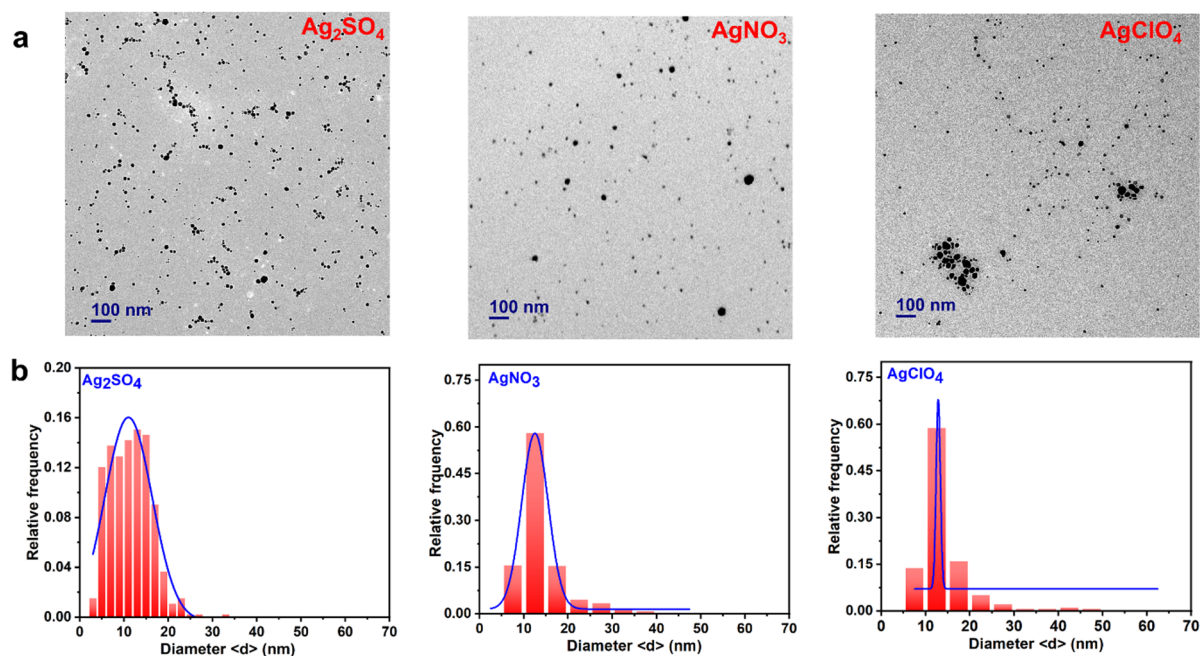
Fig. 2. (**a**) Transmission electron microscopy (TEM) images and (**b**) size distribution histograms of PVP-AgNPs synthesized using different silver precursors (Ag_2SO_4, $AgNO_3$, and $AgClO_4$) with a silver ionic concentration of 1 mM. The scale bar in the TEM images represents 100 nm.
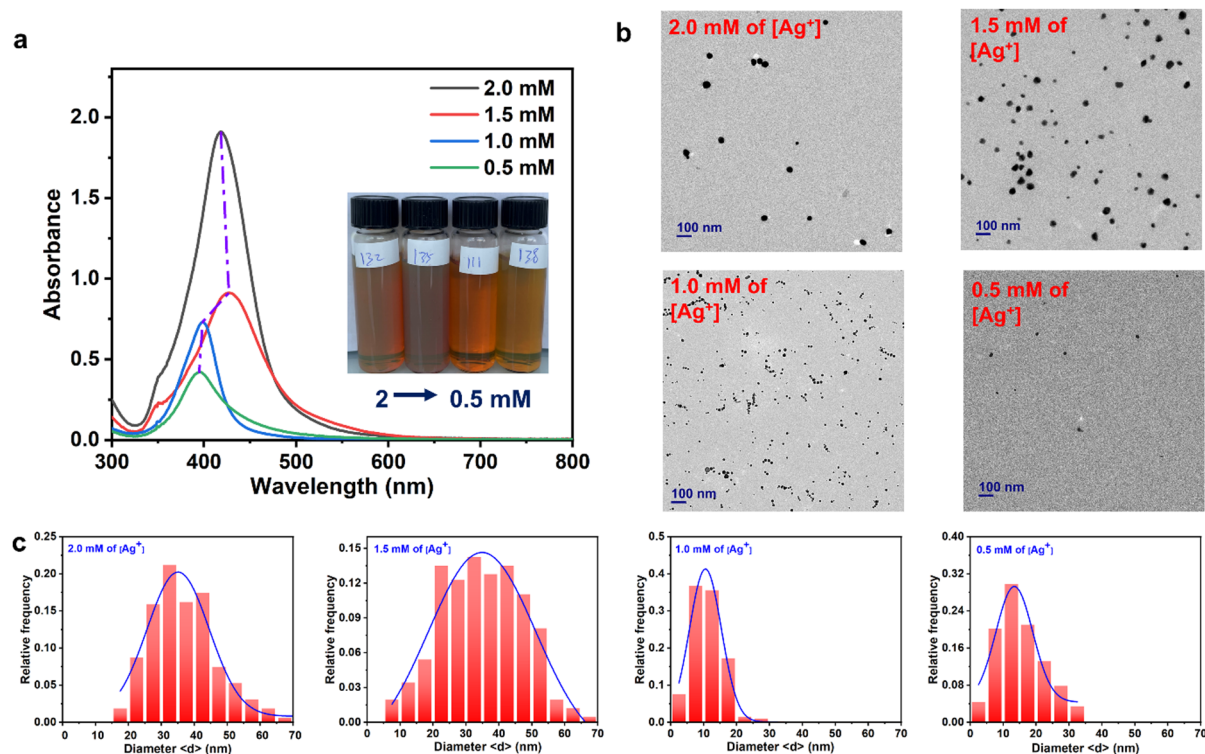
Fig. 3. (**a**) UV-Vis absorption spectra of a γ-irradiated AgNP aqueous suspension, 10-fold diluted in ultrapure water, recorded as a function of the concentration of silver ions derived from silver sulfate ([Ag⁺]) ranging from 0.5 mM to 2.0 mM. Optical path length is 1.0 c*m*. Inset: *corr*esponding optical images of pristine PVP-AgNP samples. (**b**) TEM images and (**c**) size distribution histograms of PVP-AgNPs as a function of [Ag⁺] ranging from 0.5 mM to 2.0 mM. The scale bar in the TEM images represents 100 nm.

[Ag⁺] (mM)	Absorbance (± SD)	λ_{SPR} (nm) (± SD)	FWHM (nm) (± SD)	DLS size (nm) (± SD)	PDI (± SD)
2.0	1.88 ± 0.02	416.0 ± 2.8	70.5 ± 2.1	74.1 ± 8.5	0.23 ± 0.04
1.5	0.90 ± 0.01	426.5 ± 2.1	86.5 ± 0.7	63.1 ± 3.9	0.31 ± 0.03
1.0	0.70 ± 0.07	398.3 ± 1.3	51.8 ± 5.6	45.2 ± 4.6	0.47 ± 0.05
0.5	0.42 ± 0.01	396.3 ± 0.6	70.7 ± 5.1	32.5 ± 2.2	0.59 ± 0.03

Table 2. Comparison of absorbances, absorption peaks (λ_{SPR}, nm), full width at half maximum (FWHM, nm), DLS size (nm), and PDI of PVP-AgNPs (10-fold diluted in ultrapure water) as a function of silver ion concentration ([Ag⁺]) ranging from 0.5 mM to 2.0 mM.

of some e_{aq}^- by NO_3^-[18,50]. In this study, AgNPs synthesized from Ag_2SO_4 exhibited good dispersion, uniform particle distribution, and smaller particle size, making them more suitable for medical applications, particularly in antimicrobial treatments.

### Influence of silver ion concentration on AgNP formation

The UV-Vis spectra of diluted PVP-AgNP aqueous suspensions were recorded in the range of 300–800 nm as a function of silver ion concentration, using Ag_2SO_4 as the silver precursor (Fig. 3a). The absorbance in the surface plasmon resonance region increased significantly from 0.42 ± 0.01 to 1.88 ± 0.02, as the silver ion concentration ([Ag⁺]) increased from 0.5 mM to 2.0 mM (Table 2). This increase suggests a greater formation of nanoparticles in the suspension. This is visually represented in the inset of Fig. 3a, showing the PVP-AgNP suspension darkening as the silver ion concentration increases. Additionally, when [Ag⁺] concentration increases, the absorption peak (λ_{SPR}) of AgNPs gradually red-shifts from 396.3 ± 0.6 nm to 416.0 ± 2.8 nm, which suggests a progressive increase in the AgNP particle size[51]. This tendency is consistent with that observed in the TEM images, which shows that PVP-AgNP size increases from 5 to 25 nm at 0.5 mM to 20–60 nm at 2.0 mM (Figs. 3b, c). When the [Ag⁺] concentration exceeds 1 mM, the absorption peaks λ_{SPR} of PVP-AgNP appear around 420 nm. These peaks are accompanied by broad full width at half maximum (FWHM) values of 70.5 ± 2.1 and 86.5 ± 0.7 nm, along with larger hydrodynamic particle sizes of 74.1 ± 8.5 and 63.1 ± 3.9 nm (Table 2). Notably, the 1.5 mM concentration exhibited a broader size distribution, with diameters ranging from 5 nm to

70 nm, indicating a mixture of very large and small particles (Fig. 3c). In contrast, at [Ag$^+$] below 1 mM, AgNPs remained well-dispersed with minimal aggregation, maintaining consistently small sizes, as confirmed by TEM images. At [Ag$^+$] of 0.5 mM, silver clusters exhibited good dispersibility and small particle sizes, possibly due to the strong steric hindrance of the PVP polymeric layer[41].

In conclusion, silver ion concentration significantly affects the size, distribution, and optical properties of PVP-AgNPs during the radiation reduction process. Higher concentrations lead to larger particles and broader distributions, while lower concentrations result in smaller, well-dispersed particles.

Role of PVP in controlling AgNP size

In this part, we systematically investigated how PVP concentration influences the controlled synthesis of AgNPs, focusing on its impact on particle morphology, size distribution, optical properties, and dispersibility. The UV-Vis absorption spectra of diluted PVP-AgNP aqueous solutions, recorded as a function of PVP concentration using Ag$_2$SO$_4$ as the precursor at 0.25 mM in the range of 300–800 nm, are shown in Fig. 4a. PVP concentration significantly influences AgNP synthesis, affecting particle morphology, size distribution, and surface plasmon resonance behavior. The UV-Vis spectra in Fig. 4a show that SPR peak intensity around 400 nm increases as PVP concentration rises from 20 mM to 100 mM. This suggests that higher PVP concentrations provide better control over the silver ion reduction process and silver cluster growth, resulting in more uniform particles. Additionally, TEM images and corresponding particle size distributions further confirm that as PVP
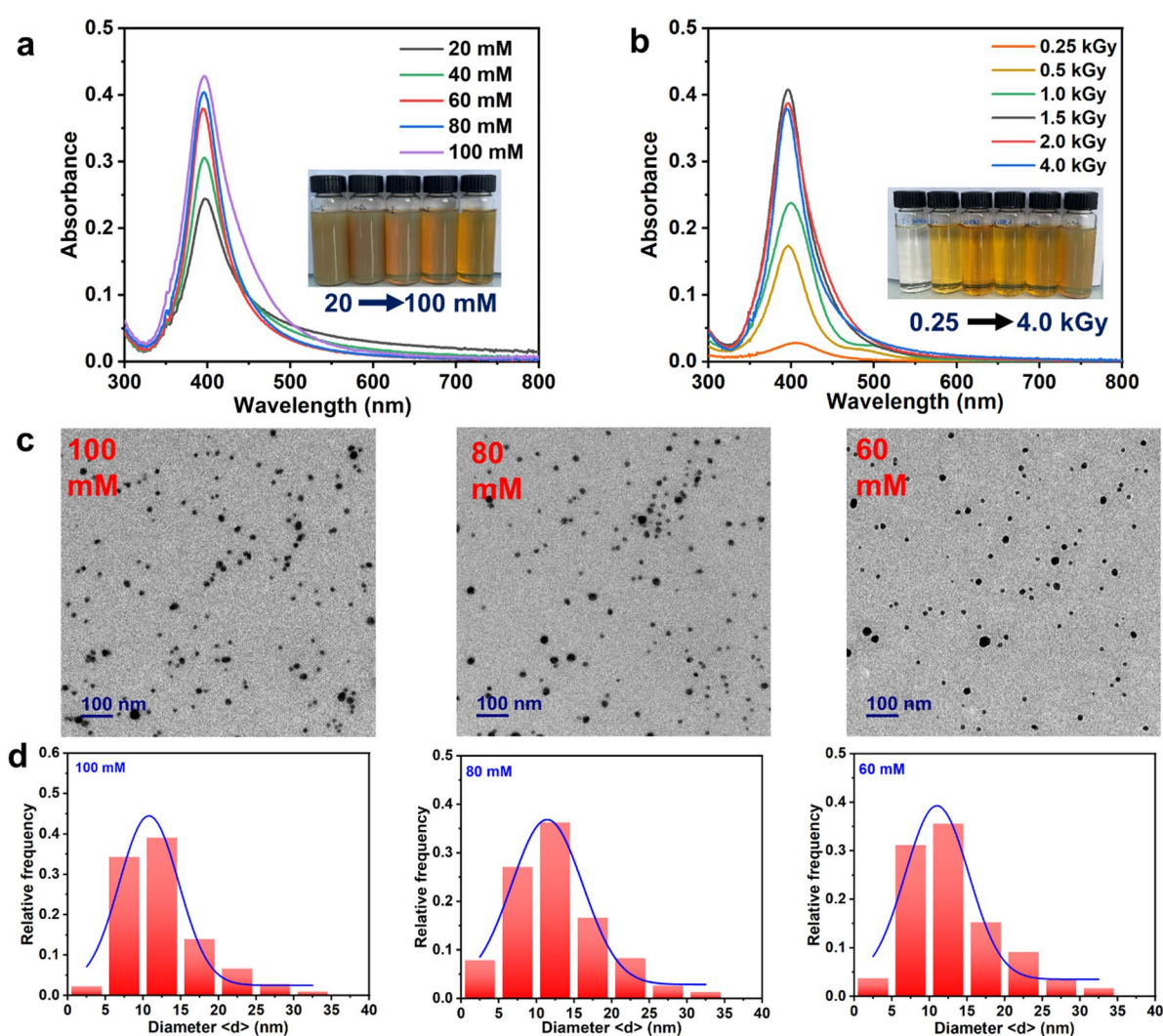
Fig. 4. UV-Vis absorption spectra of γ-irradiated AgNP aqueous suspension, recorded after 10-fold dilution in ultrapure water, as a function of (**a**) PVP concentration ranging from the monomer concentration of 20 mM to 100 mM at the total radiation doses of 2.0 kGy and (**b**) total radiation doses ranging from 0.25 kGy to 4.0 kGy at the PVP concentration of 60 mM. Optical path length is 1.0 cm. Inset: Corresponding optical images of pristine PVP-AgNP samples. (**c**) TEM images and (**d**) size distribution histograms of PVP-AgNPs separated using the Vivaspin tube with a 100 kDa cutoff, as a function of PVP concentration ranging from the monomer concentration of 60 mM to 100 mM at the total radiation doses of 2.0 kGy. The scale bar in the TEM images represents 100 nm.

concentration increases, particle size gradually decreases, and size distribution becomes slightly narrower, highlighting PVP's regulatory role in particle morphology and uniformity (Fig. 4c and d and Fig. S2). As PVP concentration increases from 20 mM to 100 mM, the FWHM of the SPR peak plateaus within the 40–80 mM range, while the absorption coefficient increases. This suggests that high PVP concentrations lead to a narrower size distribution and improve particle quality and yield. Meanwhile, the absorption peak position (λ_{SPR}) remains stable at approximately 400 nm, suggesting that concentration changes have little effect on the nanoparticles' optical properties. DLS analysis shows that as PVP concentration increases, the hydrodynamic diameter of PVP-AgNPs gradually decreases (Fig. S2). This indicates that higher PVP concentrations prevent particle aggregation, thereby enhancing dispersibility. In the light of these findings, a PVP concentration of 60 mM was selected for further studies as the best compromise between minimizing PVP usage in the synthesis and obtaining PVP-AgNPs with optimal physicochemical properties.

Impact of radiation dose on AgNP growth

As previously mentioned, the total radiation dose plays a crucial role in AgNP synthesis, primarily affecting particle size, dispersibility, and optical properties. Thus, the UV-Vis absorption spectra of diluted AgNP aqueous solutions were recorded in the range of 300–800 nm as a function of total radiation dose (Fig. 4b). As the radiation dose increases from 0.25 kGy to 4.0 kGy, the absorbance of AgNPs gradually rises before stabilizing. This suggests that higher radiation doses significantly enhance the reduction and nucleation rates of silver ions (Ag$^+$), leading to increased AgNP formation[52]. However, when the dose exceeds 1.5 kGy, the absorbance increase slows with increasing dose, likely due to the near-complete reduction of silver ions and depletion of Ag$^+$ in the reaction mixture.

Shifts in the absorption peak position (λ_{SPR}) provide insights into particle size trends. At doses ≤ 1.0 kGy, λ_{SPR} gradually redshifts, indicating the formation of larger particle, as indicated by the appearance of a second absorption peak for the irradiation doses of 0.5 and 1.0 kGy (Fig. 4b). When the dose exceeds 1.0 kGy, λ_{SPR} stabilizes, suggesting a slowdown in particle growth. Combined with DLS results, higher radiation doses result in the complete reduction of silver ions, leading to the formation of silver clusters or AgNPs, with PVP-stabilized AgNPs eventually reaching a steady state. The optimized and well-dispersed AgNPs exhibit a hydrated particle size of ~ 33 nm and a PDI of ~ 0.57 (Figure S3). Interestingly, the total radiation dose required to reduce silver ions at 0.5 mM deviates from theoretical predictions. This discrepancy may be explained by infrared spectroscopy findings, which suggests that the PVP polymer can react with the radicals induced by solvent radiolysis. This process likely enhances intra- and intermolecular hydrogen bonding, contributing to the formation of a multidimensional polymer network[53].

Structural and chemical characterization of AgNPs

Powder X-ray diffraction (PXRD) was performed to analyze the crystal structure of AgNPs synthesized in the aqueous solution (Fig. 5). Two distinct peaks at 37.1° and 44.3° (2θ) correspond to the [111] and [200] crystal planes in both AgNP samples. These findings confirm the crystallinity of the AgNPs, with face-centered cubic (**fcc**) structure of AgNPs[54], as referenced in the file No. 04-0783 of the Joint Committee on Powder Diffraction Standards (JCPDS) (Fig. 5a). The average crystalline sizes (in diameter) of optimized PVA-AgNPs and PVP-AgNPs, estimated from the [111] peak using the Scherrer equation, are ~ 9.5 nm and ~ 9.0 nm, respectively[38].

ATR-FTIR spectra recorded from 4000 to 500 cm^{-1} provide chemical insights into the as-prepared PVP- and PVA-coated AgNPs. The FTIR spectrum of PVP-AgNPs (Fig. 5b) shows C–H stretching vibrations ($\nu_{as(C-H)}$ and $\nu_{s(C-H)}$) and bending vibrations from the –CH$_2$–CH– and –CH$_2$ groups at 2949, 2919, and 2881 cm^{-1}, as well as peaks between 1493 and 1227 cm^{-1}. In PVP-AgNPs, these C–H peaks shift slightly to 2963, 2922, and 2881 cm^{-1}, along with peaks between 1494 and 1229 cm^{-1}. These shifts likely result from coordination between nitrogen and oxygen in the PVP polymer and silver in PVP-AgNPs[47]. The C = O resonance peak in the lactone amide of PVP on AgNPs shifts slightly from 1656 (free PVP) to 1654 cm^{-1}[55]. The stretching vibration of the C–C bond in the PVP skeleton chain changed to varying degrees; specifically, $\nu_{as(C-C)}$ at 895 cm^{-1}, assigned to PVP alone, shifted to 881 cm^{-1} in PVP-AgNPs. Notably, the characteristic resonance peaks of the C–N bonds in the tertiary amine group, which were originally observed at 1167, 1102, and 1071 cm^{-1} for the lactone amide of PVP alone, showed significant shifts to 1170, 1089, and 1049 cm^{-1} in PVP-AgNPs. This change can be attributed to the high affinity of nitrogen in PVP, which has multiple lone electron pairs that interact strongly with silver in PVP-AgNPs[55,56]. The broad resonance peak of PVP at 3454 cm^{-1} likely arises from absorbed water molecules and intermolecular hydrogen bonding. However, in the case of PVP-AgNPs, the corresponding peak for the stretching vibration of the O–H bond has shifted in both position and wavenumber. This change is likely due to increased intermolecular hydrogen bonding resulting from PVP chain crosslinking during ionizing radiation (Fig. 5b)[57]. Given the theoretical total radiation dose required for silver reduction, this evidence suggests that PVP chain crosslinking consumes a portion of the hydrated electrons generated by the radiolysis of water molecules.

The FTIR spectrum of PVA-AgNPs (Fig. 5c) shows an O–H stretching vibration at 3287 cm^{-1}, characteristic of polymeric O–H stretching and hydrogen bonding, likely arising from intramolecular and intermolecular interactions in the PVA polymer. This peak shifts to 3298 cm^{-1} in PVA-AgNPs. Interestingly, the stretching vibration of the C–O bond in the PVA skeleton chain shifted from 1088 to 1022 cm^{-1} to 1086 and 1046 cm^{-1} in association with PVA-AgNP. This change is probably due to the coordination bonding between the oxygen in PVA and the silver in AgNP[58]. The C–H bond stretching vibrations ($\nu_{as(C-H)}$ and $\nu_{s(C-H)}$) from the –CH$_2$–CH– group in the PVA polymer skeleton exhibited slight shifts, moving from 2938 to 2909 cm^{-1} to 2940 and 2913 cm^{-1}, which correspond to PVA-AgNPs[47].

The surface chemical states and elemental composition of silver nanoparticle (AgNP) films stabilized with PVA and PVP were systematically investigated by employing X-ray photoelectron spectroscopy. Survey spectra
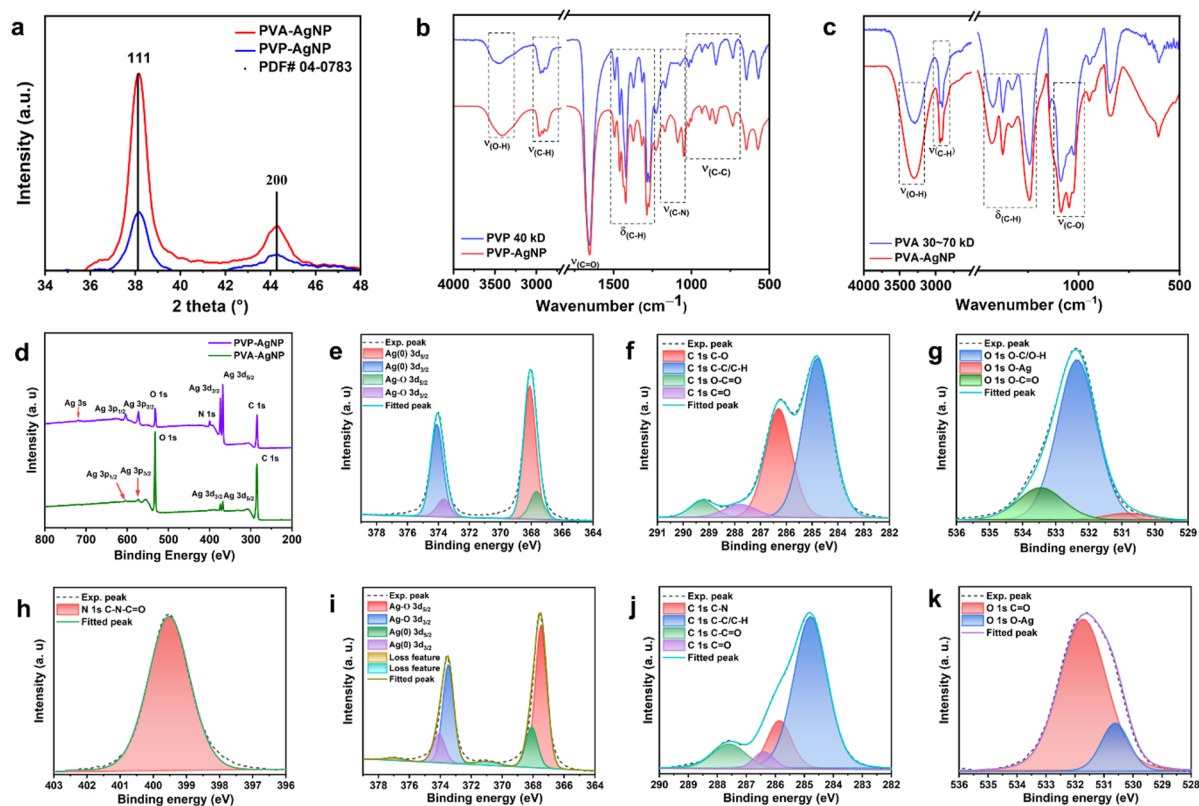
Fig. 5. Physicochemical characteristics of optimized PVP-AgNP and PVA-AgNP, in which PVP-AgNP was optimized in the condition of silver ionic concentration of 0.5 mM [Ag_2SO_4], PVP monomer concentration of 60 mM and total radiation dose of 2 kGy, and PVA-AgNP was optimized in the condition of silver ionic concentration of 2.0 mM [Ag_2SO_4], PVA monomer concentration of 100 mM and total radiation dose of 4.5 kGy. (**a**) PXRD patterns of as-prepared PVP-AgNP and PVA-AgNP in liquid phase, and further purified using a Vivaspin tube with a 100 kDa of cut-off. ATR-FTIR spectra of: (**b**) PVP-AgNP and PVP polymer alone and (**c**) PVA-AgNP and PVA polymer alone, recorded in the wavenumber range of 4000–500 cm^{-1}. (**d**) XPS survey spectra analysis of PVP-AgNP and PVA-AgNP. Core-level spectra and chemical state assessment of (**e**) Ag 3d, (**f**) C 1s, (**g**) O 1s in PVA-AgNP and (**h**) N 1s (**i**) Ag 3d, (**j**) C 1s, (**k**) O 1s in PVP-AgNP.

demonstrated prominent signals corresponding to Ag, O, and C elements in both samples, while a distinct N 1s peak, attributed to the pyrrolidone moiety in PVP, was observed exclusively in PVP-AgNPs. These observations confirm the successful functionalization of AgNPs with each polymer.

Core-level Ag 3d spectra for both PVA- and PVP-stabilized AgNPs revealed characteristic spin-orbit doublets at 368.1 eV for Ag $3d_{5/2}$ and 374.1 eV for Ag $3d_{3/2}$, with a splitting step of 6.0 eV, indicating the presence of metallic silver (Figs. 5e, i)[59]. Notably, metallic Ag (0), accounting for 82.7%, is the main chemical state on the PVA-stabilized AgNPs, indicating that the PVA coating has excellent antioxidant protection. To further support the identification of metallic silver in AgNPs, the Ag Auger (MNN) spectra in Figure S4d show kinetic energies and Auger parameters consistent with metallic Ag, confirming its predominant chemical state[60]. Additionally, in the case of C 1s core level spectrum of the PVA-AgNP (Fig. 5f), four peaks are considered to be C–C/C–H (284.8 eV), C–O (286.3 eV), C = O (287.8 eV), and O–C = O (289.3 eV). Among them, the O–C = O peak at ~ 289.3 eV originates from the incompletely hydrolyzed pure PVA polymer (87–90% hydrolyzed) (Figure S4b). Additionally, partial oxidation of the hydroxyl groups during film formation contributed to the C = O signal. The O 1s core-level spectrum (Fig. 5g) shows that in addition to the main O–H peak at 532.3 eV, the Ag–O peak at 530.4 eV, accounting for 4%, further indicates the formation of coordination bonds or other interactions between Ag and the functional groups in the PVA molecules, and may partly come from the Ag_2O on the surface of the PVA-AgNP film, considering that XPS is a surface-sensitive spectroscopic technique[61,62]. In the case of PVP-AgNP, the proportion of the Ag–O peak reaches 77.9%, which is probably attributed to the formation of strong coordination bonds or other interactions between Ag and the carbonyl groups in the PVP molecules, as well as the oxidation process of the PVP-AgNP film formed by the smaller particles of PVP-AgNP[61]. Also, subsequent long-term stability measurements showed that the colloidal stability of PVP-AgNP is weaker than that of PVA-AgNP (Fig. 5). The core-level C spectrum of PVP-AgNP was considered into C–C/C–H (284.8 eV), C–N (285.9 eV), C–C = O (287.6), and C = O (286.4 eV) of different carbon chemical states in PVP (Fig. 5j). These peaks shifted slightly compared to pure PVP molecules, reflecting the structural characteristics of PVP and its interaction with Ag clusters' surface[63]. Additionally, the presence of organic oxygen species and Ag_2O was further confirmed by the O 1s spectrum. The peak at ~ 531.8 eV was attributed to the carboxyl oxygen (C

= O) in the PVP molecule, which was shifted to be higher binding energy compared to the carboxyl (C = O) oxygen in pure PVP (531.3 eV), indicating that the electron density around the carboxyl (C = O) oxygen was reduced[64]. The N (1s) peak of PVP-AgNP at 399.5 eV was slightly and negatively shifted compared to that in pure PVP molecules, indicating that the N atom was affected by the final state effect of the core silver clusters[65]. In conclusion, different surface chemical environments imparted by different stabilizers are expected to affect the physicochemical properties of AgNPs and their potential applications in antimicrobial activity and other areas.

Colloidal stability of AgNPs

Assessing the colloidal stability of AgNPs under different temperatures, including low and physiological conditions, is essential for understanding their biomedical performance and optimizing storage and transportation. Flattened waterfall plots of UV-Vis spectra for optimized PVP-AgNP and PVA-AgNP in short-term (12 h) and long-term (1 month) stability tests are shown in Fig. 6, where both samples were stored in amber glass under ambient air conditions. These plots illustrate the colloidal stability of AgNPs under different temperatures and incubation times, highlighting their dynamic changes. The results indicate that temperature is a key factor affecting AgNP colloidal stability. In short-term stability tests, both PVP- and PVA-stabilized AgNPs remained highly stable at 4 °C, as indicated by relatively constant absorbance and a stable maximum absorption peak. This suggests good dispersion and colloidal stability at 4 °C. In contrast, absorbances of both AgNPs slightly decreased at 25 °C and 37 °C, and the maximum absorption peak redshifted gradually, with more pronounced effects at 37 °C for PVP-AgNP. DLS measurements confirm that the hydrodynamic diameter and PDI values increased significantly at 37 °C (Figs. S5, S7), indicating substantial NP aggregation or degradation, which can be attributed to temperature-induced factors such as enhanced surface atom mobility leading to particle agglomeration and oxidative processes reducing nanoparticle stability[66,67].

In long-term stability tests, higher temperatures had a more pronounced negative impact on colloidal stability. At 4 °C, both absorbance at λ_{SPR} and hydrodynamic diameters remained stable (Figs. S6, S8). In contrast, the absorbance declined significantly over time at 25 °C and 37 °C. Particularly, at 37 °C, the absorption peak for PVP-AgNP dropped sharply and redshifted slightly, suggesting potential particle degradation or reorganization[67]. These findings suggest that at elevated temperatures, stabilizing agents (PVP or PVA) may partially lose effectiveness, reducing electrostatic repulsion and steric hindrance between particles[14,67]. Overall, the findings demonstrate that AgNPs exhibit optimal colloidal stability at low temperatures (4 °C), while higher
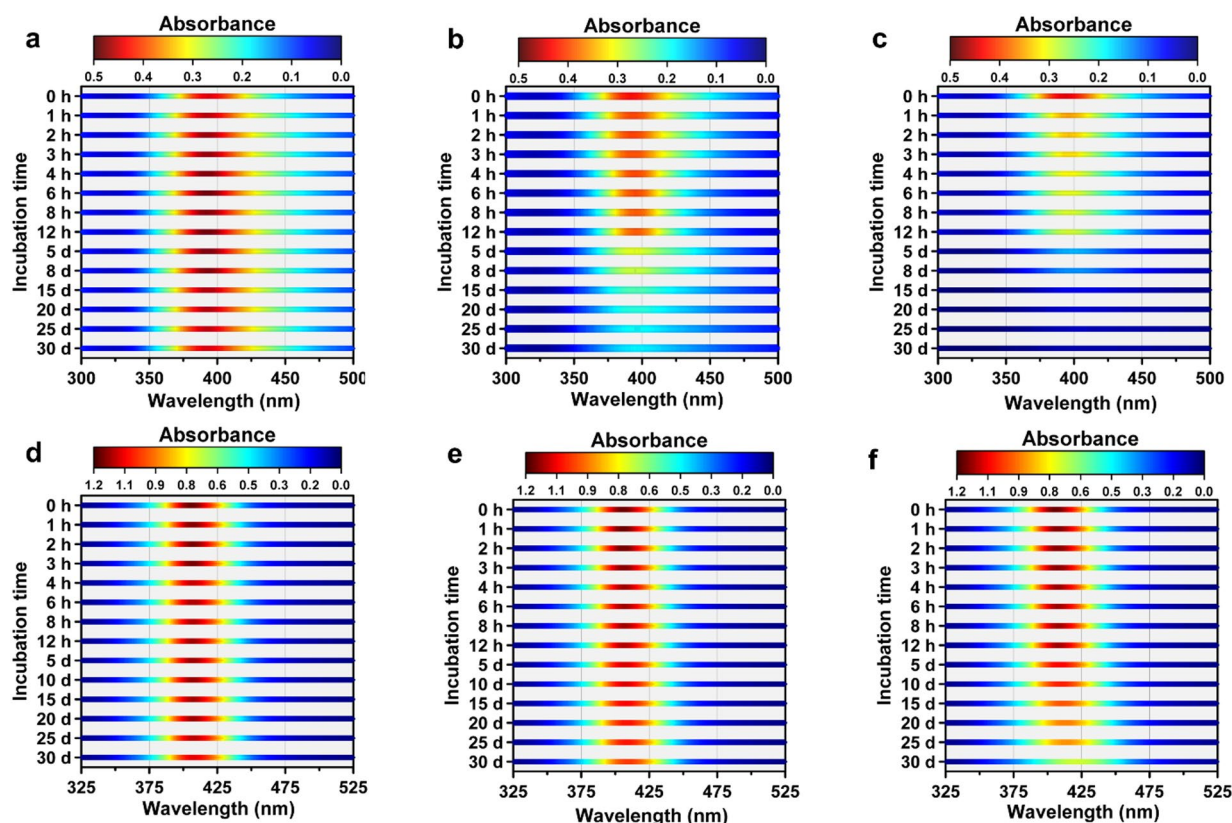
Fig. 6. Ultraviolet-visible absorption spectra presented as flattened waterfall plots, illustrating the colloidal stability of (**a–c**) PVP-AgNP aqueous suspensions (10-fold diluted in ultrapure water) and (**d–f**) PVA-AgNP aqueous suspensions (20-fold diluted in ultrapure water) as a function of incubation time at three different temperatures of 4, 25, and 37 °C from left to right.
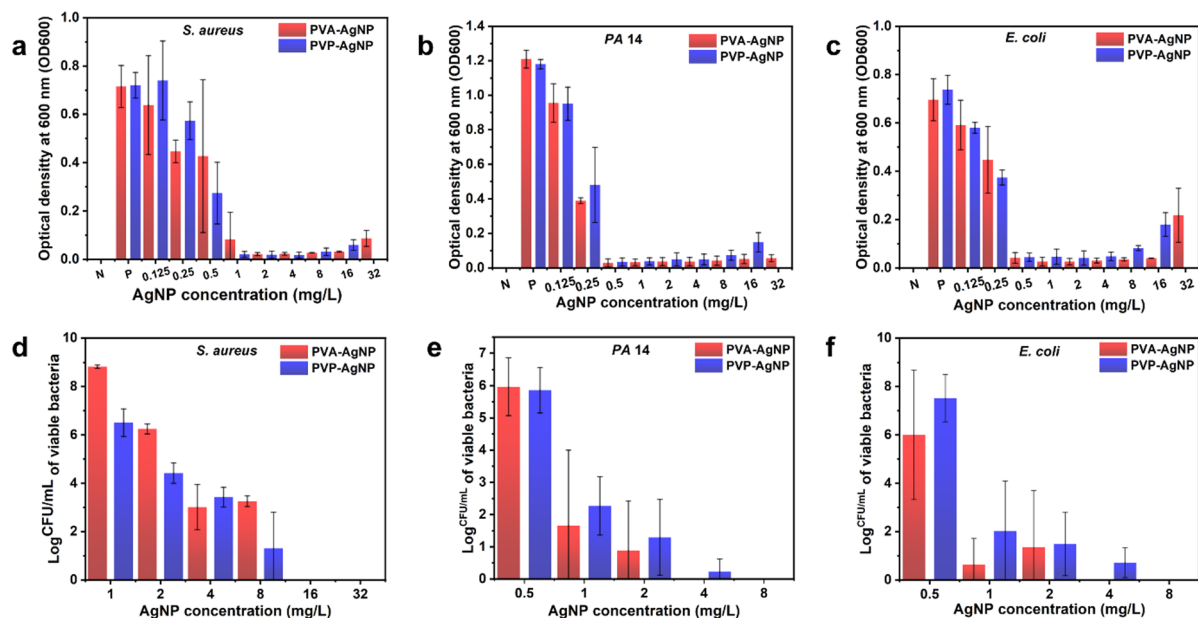
Fig. 7. Comparative antibacterial activity of PVA-AgNP and PVP-AgNP against *S. aureus* ATCC 27217 (**a**, **d**), *P. aeruginosa* PA14 (**b**, **e**) and *E. coli* MG1655 (**c**, **f**) based on optical density (OD_{600}) and viability assays. "N" denotes the negative control (MHB-CA broth alone), while "P" represents the positive control (bacterial culture without treatment).

	PVA-AgNP				PVP-AgNP			
	MIC_{1st}	MIC_{2nd}	MIC_{3rd}	MIC_{mean}	MIC_{1st}	MIC_{2nd}	MIC_{3rd}	MIC_{mean}
S. aureus ATCC 27217	2	1	1	1 ~ 2	1	1	1	1
P. aeruginosa PA14	0.5	0.5	0.5	0.5	0.5	0.5	0.5	0.5
E. coli MG1655	0.5	0.5	0.5	0.5	0.5	0.5	0.5	0.5

Table 3. Comparative analysis of minimum inhibitory concentration (MIC, mg/L) of PVA-AgNPs and PVP-AgNPs against *S. aureus* ATCC 27217, *P. aeruginosa* PA14 and *E. coli* MG1655.

	PVA-AgNP				PVP-AgNP			
	MBC_{1st}	MBC_{2nd}	MBC_{3rd}	MBC_{mean}	MBC_{1st}	MBC_{2nd}	MBC_{3rd}	MBC_{mean}
S. aureus ATCC 27217	16	16	16	16	16	8	16	8 ~ 16
P. aeruginosa PA14	2	2	1	1 ~ 2	2	2	1	1 ~ 2
E. coli MG1655	1	4	1	1 ~ 4	1	2	2	1 ~ 2

Table 4. Comparative analysis of minimum bactericidal concentration (MBC, mg/L) of PVA-AgNPs and PVP-AgNPs against *S. aureus* ATCC 27217, *P. aeruginosa* PA14 and *E. coli* MG1655.

temperatures promote destabilization and/or degradation. At high temperatures, PVP-AgNPs exhibit lower colloidal stability than PVA-AgNPs, likely due to their smaller particle size and lower stabilizer content.

Antibacterial activity of AgNPs

In this study, antimicrobial efficacies of two AgNP nanocomposites (PVA-AgNP and PVP-AgNP) were systematically evaluated against three different bacterial strains as models (*S. aureus* ATCC 27217, *P. aeruginosa* PA14, and *E. coli* MG1655) at the NPs' concentration ranging from 0.125 to 32 mg/L (Fig. 7; Tables 3 and 4). Bacterial growth and viability under the treatment of AgNP nanocomposites were assessed using optical density (OD_{600}) and bacterial viable count (log CFU/mL) measurements, respectively. Antibacterial activities across three bacterial strains revealed a clear dose-dependent antibacterial effect exhibited by both AgNPs.

As shown in Figs. 7a–c, the OD$_{600}$ values, indicative of bacterial growth, decreased significantly with increasing concentrations of AgNP composites. For the pathogenic Gram-positive strain *S. aureus* ATCC 27217, complete growth inhibition was achieved at 1 mg/L for PVP-AgNP and 1–2 mg/L for PVA-AgNP (Table 3). In contrast, lower minimum inhibitory concentrations of 0.5 mg/L were observed for Gram-negative strains of *P. aeruginosa* PA14 and *E. coli* MG1655 (Table 3).

Both PVP-AgNPs and the larger PVA-AgNPs exhibited stronger inhibitory effects on Gram-negative bacteria at lower concentrations, likely attributable to the contrasting architecture of the bacterial cell envelope between Gram-positive and Gram-negative bacteria, as illustrated in Fig. 8. Specifically, Gram-negative bacteria are protected by a dual-membrane system comprising an outer membrane densely packed with lipopolysaccharide (LPS) and interspersed with porins, as well as an underlying thin peptidoglycan layer (2–3 nm)[68]. This could facilitate the adhesion of the nanoparticles to the surface of Gram-negative cells, resulting in a locally elevated Ag$^+$ concentration at the outer membrane interface[69].

Furthermore, in previous colloidal stability tests, PVP-AgNPs with a higher specific surface area than the PVA-AgNPs were observed to be more susceptible to destabilization at 37 °C. Such instability may further accelerate the release of silver ions. Once released, Ag$^+$ could traverse the 1–2 nm porins, entering the periplasmic space. After crossing the thin peptidoglycan barrier, Ag$^+$ could exert an antibacterial action by interfering with respiratory enzymes and generating reactive oxygen species[70,71]. By contrast, Gram-positive bacteria lack an outer membrane but possess a substantially thicker and highly porous peptidoglycan layer (> 20 nm) interwoven with teichoic acids that could impede AgNPs penetration. Additionally, teichoic acids could further chelate silver ions within the cell wall, delaying their arrival at the cytoplasmic membrane[71]. For instance, interactions between green-synthesized AgNPs (G-AgNPs, using leaf extracts) and pathogenic bacteria were investigated by atomic force microscopy[72], revealing that G-AgNPs accumulate on bacterial surfaces via electrostatic or hydrophobic interactions, triggering oxidative stress and metabolic collapse. Notably, G-AgNPs demonstrated selective affinity for Gram-negative bacteria like *E. coli*, where nanoscale penetration and increased membrane roughness critically compromise structural integrity. In contrast, the thick peptidoglycan layer of Gram-positive bacteria like *S. aureus* impedes nanoparticle penetration, necessitating higher AgNP concentrations for bactericidal activity.

The dose-dependent bactericidal effects of both AgNPs were further corroborated by plate-counting assays (Figs. 7d–f). These results also highlighted the impact of structural differences between Gram-positive and Gram-negative bacteria on their susceptibility to AgNPs. For *S. aureus* ATCC 27217 system, treatments with PVA- and PVP-AgNP at 16 mg/L and 8–16 mg/L, respectively, reduced the viable bacterial counts by three orders of magnitude, compared to the initial bacterial density (Table 4). At higher concentrations, both materials achieved complete eradication of the bacteria. For *P. aeruginosa* PA14 and *E. coli* MG1655 (Figs. 7e, f), significant reductions in viable bacteria were observed even at 2 mg/L, as evidenced by the substantially lower bacterial counts compared to the initial density. Notably, PVP-AgNP demonstrated slightly higher bactericidal efficacy at lower doses than PVA-AgNP, potentially due to its smaller nanoparticle size facilitating enhanced penetration into Gram-negative bacteria and Gram-positive bacteria employed in this study (Fig. 8)[15,73]. Besides, previous investigations have shown that smaller AgNPs show higher antibacterial activity than larger ones. While AgNPs of 20–80 nm mainly act *via* oxidative dissolution and Ag$^+$ release, 10 nm AgNPs exhibit markedly greater toxicity against *E. coli*. Their reduced size allows closer contact with bacterial cells, enhancing internalization, silver ion
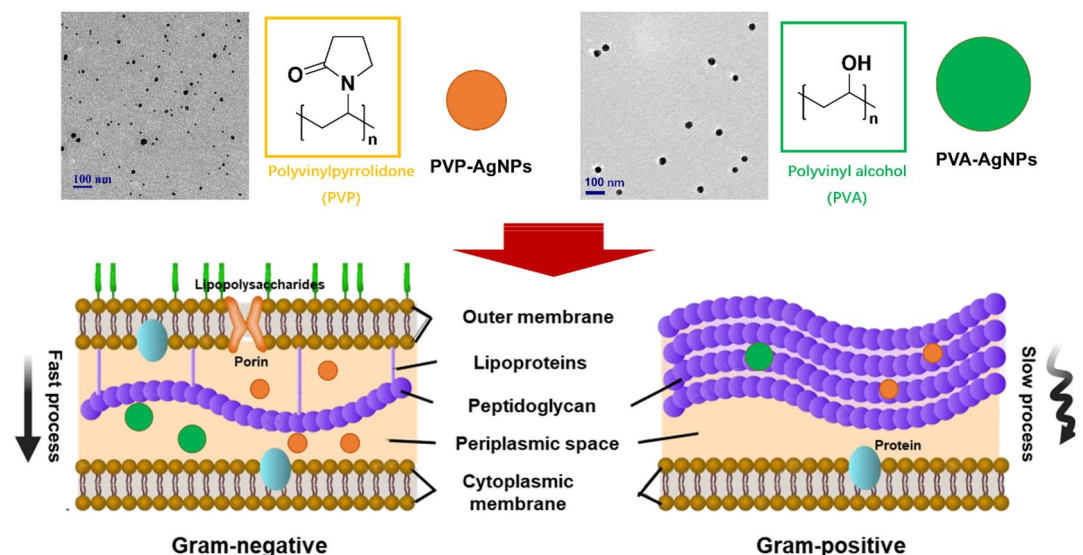
Fig. 8. Schematic representation of the proposed size-dependent antibacterial mechanisms of PVP- and PVA-stabilized AgNPs. Smaller AgNPs (TEM insets) are presumed to penetrate more easily through the outer membrane/porins and thin peptidoglycan layer of Gram-negative bacteria. In contrast, in Gram-positive bacteria, the thick peptidoglycan layer hinders nanoparticle access.
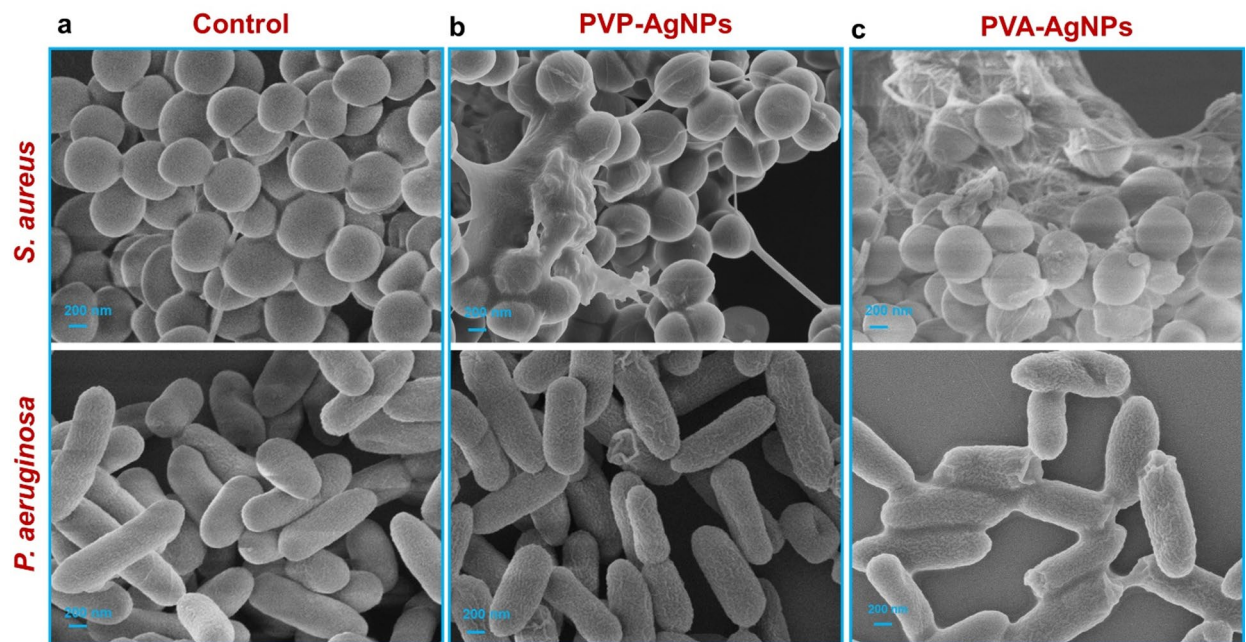
Fig. 9. SEM comparison of ultrastructural alterations in *S. aureus* and *P. aeruginosa* following exposure to different AgNPs at their respective MICs. (**a**) Control group; (**b**) Treated with PVP-AgNPs; (**c**) Treated with PVA-AgNPs. The scale bar in the SEM images is 200 nm.

release, and free radical generation. This size-dependent effect makes smaller AgNPs more efficient at disrupting bacterial cells[69,72,74].

Besides, additional antibacterial investigation of non-AgNP components in the composites confirmed that the broad-spectrum antimicrobial activity of both PVP-AgNP and PVA-AgNP against all three strains originated exclusively from the AgNP fraction (Figure S9). Furthermore, although the optical scattering effect of silver nanocomposites at high concentrations led to elevated OD_{600} values associated with bacterial density, bacterial growth was fully suppressed at these concentrations, as evidenced by CFU data.

SEM observation of bacterial morphology

SEM was employed to observe the possible morphological alterations in the bacterial cells. As shown in Fig. 9, SEM images reveal distinct morphological alterations in both *S. aureus* and *P. aeruginosa* following exposure to PVP-AgNPs and PVA-AgNPs, respectively, compared with untreated controls. Untreated S. *aureus* and *P. aeruginosa* displayed characteristic intact morphologies (Fig. 9a): *S. aureus* in the control group exhibits smooth, complete grape-like cocci while *P. aeruginosa* possesses uniform rods with continuous, undamaged surfaces. In contrast, bacteria treated with both PVP-AgNPs and PVA-AgNPs exhibited severe surface modifications, deposits and/or deformations, suggesting the onset of envelope stress and disruption. These morphological changes indicate that polymer-stabilized AgNPs can induce substantial structural damage to both Gram-positive and Gram-negative bacteria.

AgNPs and silver-based nanocomposites have been extensively utilized in medical, food processing, textile, and environmental management applications due to their remarkable antimicrobial properties[75]. Their broad-spectrum antibacterial activity primarily stems from their unique physicochemical characteristics and diverse bactericidal mechanisms[3,14]. Metallic silver at the nanoscale of 1–100 nm exhibits exceptionally high surface energy and specific surface area. The size-dependent effect significantly enhances interactions with microbial cells, enabling effective adhesion to cell membranes and even penetration into intracellular environments. The antibacterial efficacy of silver-based materials is closely linked to the sustained release of Ag^+. Notable mechanisms include disruption of bacterial membrane structures, interference with DNA replication and gene expression, inactivation of essential proteins, and induction of intracellular oxidative stress, all of which synergistically amplify antimicrobial effects[15,76]. In addition to Ag^+ release, AgNPs themselves exert direct physical damage by binding to bacterial surfaces, altering membrane fluidity, integrity, and permeability, ultimately leading to cell death. Recently, the formulation of Ag^+-coordinated Fmoc-amino acid metallohydrogel, reported by Yan et al.[77], leveraged the synergistic effects of Ag^+ release and Fmoc-amino acids to disrupt bacterial membrane integrity while generating reactive oxygen species (ROS), thereby damaging DNA and protein functionality. Furthermore, the in-situ synthesis of ultrasmall AgNPs (< 6 nm) uniformly dispersed within hydrogel fibers exhibited enhanced membrane permeability through hydrophobic interactions with amino acids. These AgNPs demonstrated effective penetration across both Gram-negative and Gram-positive bacterial cell walls, achieving broad-spectrum antimicrobial efficacy.

Compared to conventional antibiotics, AgNPs act on multiple antibacterial targets, making it difficult for bacteria to develop resistance through single mutations or adaptive mechanisms[15,78]. Moreover, studies

have shown that some antibacterial materials like AgNPs exhibit notable synergistic effects when combined with conventional antibiotics, a phenomenon known as "antibiotic synergism", which significantly enhances antimicrobial performance[79]. One of our future research objectives is to develop multifunctional platforms combining AgNPs, photoactive antimicrobial materials, and antibiotics. Such strategies aim to reduce bacterial resistance, mitigate potential cytotoxicity of silver-based materials, and advance silver nanocomposites as leading candidates for next-generation broad-spectrum antimicrobial applications.

Conclusion

In response to the escalating global threat of AMR, this study presents a green, efficient, and scalable strategy for synthesizing AgNPs via gamma radiation-assisted reduction in aqueous media, using PVP or PVA as stabilizers. This approach eliminates the need for toxic chemical reducing agents and enables direct, sterile production of AgNPs, making it highly suitable for biomedical applications. Systematic investigations revealed that the choice of silver precursor and stabilizer critically influences the physicochemical properties and antimicrobial efficacy of AgNPs. Notably, AgNPs synthesized from Ag_2SO_4 exhibited smaller, more uniform particle sizes and superior optical properties compared to those derived from $AgNO_3$ or $AgClO_4$. Comprehensive characterization by TEM, UV-Vis, PXRD, FTIR, XPS, and DLS confirmed the crystalline structure, surface chemistry, and colloidal stability of the optimized AgNPs. PVP-AgNPs displayed a classic surface plasmon resonance at ~ 396 nm, a narrow size distribution (5–25 nm by TEM), and a hydrated diameter of ~ 33 nm. Both PVP- and PVA-stabilized AgNPs demonstrated excellent colloidal stability for at least 1 month at 4 °C. PVA-AgNPs showed enhanced long-term stability due to higher metallic silver content and stronger antioxidant protection. Notably, both AgNPs composites exhibited potent, broad-spectrum antibacterial activity against clinically relevant Gram-positive (*S. aureus*) and Gram-negative (*P. aeruginosa, E. coli*) pathogens, with MICs as low as 0.5 mg/L for Gram-negative strains and 1–2 mg/L for *S. aureus*. The enhanced efficacy against Gram-negative bacteria is attributed to their thinner peptidoglycan layer, facilitating AgNPs penetration and bactericidal action. Overall, this work provides a robust theoretical and technical foundation for the green synthesis of high-performance, stable, and environmentally friendly AgNP-based antimicrobial materials. The gamma radiation-assisted method not only ensures precise control over NP properties and inherent sterility, but also paves the way for the development of next-generation antimicrobial platforms to combat AMR. The radiolytic process is reproducible, green and scalable and many industries in France and all over the world are selling irradiations for different application such as sterilizations of food, surgical materials and medicines.

Data availability

The data that support the findings of this study are available from the corresponding author upon reasonable request. Please contact Ruxandra Gref at ruxandra.gref@cnrs.fr.

References

1. Pendleton, J. N., Gorman, S. P. & Gilmore, B. F. Clinical relevance of the ESKAPE pathogens. *Expert Rev. Anti Infect. Ther.* **11**, 297–308 (2013).
2. Organization, W. H. & Interagency Coordination Group on Antimicrobial Resistance. *No time to wait: securing the future from drug-resistant infections, Report to the secretary-general of the united nations* 1, 28 (2019).
3. Santajit, S. & Indrawattana, N. Mechanisms of Antimicrobial Resistance in ESKAPE Pathogens. *Biomed Res. Int.* **2016**, 2475067 (2016).
4. De Oliveira, D. M. P. et al. Antimicrobial resistance in ESKAPE pathogens. *Clin. Microbiol. Rev.* **33**, 10–1128 (2020).
5. Poole, K. Resistance to β-lactam antibiotics. *CMLS Cell. Mol. Life Sci* **61** (2004).
6. Arnold, B. J., Huang, I. T. & Hanage, W. P. Horizontal gene transfer and adaptive evolution in bacteria. *Nat. Rev. Microbiol.* **20**, 206–218 (2022).
7. Zhou, Z. et al. Quaternary ammonium salts: insights into synthesis and new directions in antibacterial applications. *Bioconjug. Chem.* **34**, 302–325 (2023).
8. Yu, H. et al. Water-Insoluble polymeric guanidine derivative and application in the Preparation of antibacterial coating of catheter. *ACS Appl. Mater. Interfaces.* **10**, 39257–39267 (2018).
9. Jeong, C. J., Sharker, S., Md., In, I. & Park, S. Y. Iron Oxide@PEDOT-Based recyclable photothermal nanoparticles with Poly(vinylpyrrolidone) sulfobetaines for rapid and effective antibacterial activity. *ACS Appl. Mater. Interfaces.* **7**, 9469–9478 (2015).
10. Wang, Y. et al. Antimicrobial blue light inactivation of pathogenic microbes: state of the Art. *Drug Resist. Updates.* **33–35**, 1–22 (2017).
11. Zhang, L. & Gallo, R. L. Antimicrobial peptides. *Curr. Biol.* **26**, R14–R19 (2016).
12. Perreault, F., de Faria, A. F., Nejati, S. & Elimelech, M. Antimicrobial properties of graphene oxide nanosheets: why size matters. *ACS Nano.* **9**, 7226–7236 (2015).
13. Zhao, C. et al. Quaternized carbon quantum Dots with broad-spectrum antibacterial activity for the treatment of wounds infected with mixed bacteria. *Acta Biomater.* **138**, 528–544 (2022).
14. Haidari, H. et al. Ultrasmall AgNP-Impregnated biocompatible hydrogel with highly effective biofilm elimination properties. *ACS Appl. Mater. Interfaces.* **12**, 41011–41025 (2020).
15. Tang, S. & Zheng, J. Antibacterial activity of silver nanoparticles: structural effects. *Adv. Healthc. Mater.* **7**, 1701503 (2018).
16. Sánchez-López, E. et al. Metal-Based nanoparticles as antimicrobial agents: an overview. *Nanomaterials* **10**, 292 (2020).
17. Barillo, D. J. & Marx, D. E. Silver in medicine: A brief history BC 335 to present. *Burns* **40**, S3–S8 (2014).
18. Menéndez Miranda, M. et al. Colloidal silver nanoparticles obtained via radiolysis: synthesis optimization and antibacterial properties. *Pharmaceutics* **15**, 1787 (2023).
19. Nqakala, Z. B. et al. Advances in nanotechnology towards development of silver Nanoparticle-Based Wound-Healing agents. *Int. J. Mol. Sci.* **22**, 11272 (2021).
20. Murphy, M., Ting, K., Zhang, X., Soo, C. & Zheng, Z. Current development of silver nanoparticle preparation, investigation, and application in the field of medicine. *J. Nanomater.* **2015**, 696918 (2015).

21. Raj, S., Trivedi, R. & Soni, V. Biogenic synthesis of silver Nanoparticles, characterization and their Applications—A review. *Surfaces* **5**, 67–90 (2022).
22. Remita, H. & Remita, S. Metal clusters and nanomaterials: Contribution of radiation chemistry. in *Recent Trends in Radiation Chemistry* 347–383 (WORLD SCIENTIFIC, 2010).
23. Shaheen, M. N. F., El-hadedy, D. E. & Ali, Z. I. Medical and microbial applications of controlled shape of silver nanoparticles prepared by ionizing radiation. *BioNanoScience* **9**, 414–422 (2019).
24. Buxton, G. V., Greenstock, C. L., Helman, W. P. & Ross, A. B. Critical review of rate constants for reactions of hydrated electrons, hydrogen atoms and hydroxyl radicals ($\cdot OH/\cdot O-$ in aqueous solution. *J. Phys. Chem. Ref. Data.* **17**, 513–886 (1988).
25. Remita, H. & Lampre, I. Synthesis of metallic nanostructures using ionizing radiation and their applications. *Materials* **17**, 364 (2024).
26. Remita, H., Lampre, I., Mostafavi, M., Balanzat, E. & Bouffard, S. Comparative study of metal clusters induced in aqueous solutions by γ-rays, electron or C6 + ion beam irradiation. *Radiat. Phys. Chem.* **72**, 575–586 (2005).
27. Mansour, H., Eid, M. & El-Arnaouty, M. Effect of silver nanoparticles synthesized by gamma radiation on the cytotoxicity of doxorubicin in human cancer cell lines and experimental animals. *Hum. Exp. Toxicol.* **37**, 38–50 (2018).
28. Alcântara, M. T. S. et al. Simultaneous hydrogel crosslinking and silver nanoparticle formation by using ionizing radiation to obtain antimicrobial hydrogels. *Radiat. Phys. Chem.* **169**, 108777 (2020).
29. Cui, Z. et al. A novel radiation chemistry-based methodology for the synthesis of PEDOT/Ag nanocomposites. *Mater. Chem. Front.* **1**, 879–892 (2017).
30. Ray, P. et al. Stabilisation of small mono- and bimetallic gold–silver nanoparticles using calix[8]arene derivatives. *New. J. Chem.* **42**, 14128–14137 (2018).
31. Belloni, J., Mostafavi, M., Remita, H., Marignier, J. L. & Delcourt, A. M.-O. Radiation-induced synthesis of mono- and multi-metallic clusters and nanocolloids. *New. J. Chem.* **22**, 1239–1255 (1998).
32. Méndez-Medrano, M. G. et al. Inhibition of fungal growth using modified TiO2 with Core@Shell structure of Ag@CuO clusters. *ACS Appl. Bio Mater.* **2**, 5626–5633 (2019).
33. Tausch-Treml, R., Henglein, A. & Lilie, J. Reactivity of silver atoms in aqueous solution II. A pulse radiolysis study. *Ber Bunsenges Phys. Chem.* **82**, 1335–1343 (1978).
34. Mulvaney, P. & Henglein, A. Formation of unstabilized oligomeric silver clusters during the reduction of Ag + ions in aqueous solution. *Chem. Phys. Lett.* **168**, 391–394 (1990).
35. Chaudhuri, B., Mondal, B., Ray, S. K. & Sarkar, S. C. A novel biocompatible conducting Polyvinyl alcohol (PVA)-polyvinylpyrrolidone (PVP)-hydroxyapatite (HAP) composite scaffolds for probable biological application. *Colloids Surf. B: Biointerfaces.* **143**, 71–80 (2016).
36. Rogero, S. O. et al. Biocompatibility study of polymeric biomaterials. *Artif. Organs.* **27**, 424–427 (2003).
37. He, J. et al. The broad host range pathogen Pseudomonas aeruginosa strain PA14 carries two pathogenicity Islands harboring plant and animal virulence genes. *Proc. Natl. Acad. Sci. U S A.* **101**, 2530–2535 (2004).
38. Patterson, A. L. The scherrer formula for X-Ray particle size determination. *Phys. Rev.* **56**, 978–982 (1939).
39. Schön, T. et al. Antimicrobial susceptibility testing of Mycobacterium tuberculosis complex isolates – the EUCAST broth microdilution reference method for MIC determination. *Clin. Microbiol. Infect.* **26**, 1488–1492 (2020).
40. Peterson, L. R. & Shanholtzer, C. J. Tests for bactericidal effects of antimicrobial agents: technical performance and clinical relevance. *Clin Microbiol. Rev* **5** (1992).
41. Koczkur, K. M., Mourdikoudis, S., Polavarapu, L. & Skrabalak, S. E. Polyvinylpyrrolidone (PVP) in nanoparticle synthesis. *Dalton Trans.* **44**, 17883–17905 (2015).
42. Pasparakis, G. Recent developments in the use of gold and silver nanoparticles in biomedicine. *Wiley Interdiscip Rev. Nanomed. Nanobiotechnol.* **14**, e1817 (2022).
43. Čubová, K. & Čuba, V. Synthesis of inorganic nanoparticles by ionizing radiation – a review. *Radiat. Phys. Chem.* **169**, 108774 (2020).
44. Schwarz, H. A. Free radicals generated by radiolysis of aqueous solutions. *J. Chem. Educ.* **58**, 101 (1981).
45. Mu, S. et al. Hydroxyl radicals dominate reoxidation of oxide-derived Cu in electrochemical CO2 reduction. *Nat. Commun.* **13**, 3694 (2022).
46. Lungulescu, E. M. et al. Gamma Radiation-Mediated synthesis of antimicrobial polyurethane Foam/Silver nanoparticles. *Polymers* **16**, 1369 (2024).
47. Garcia, A. M., Martins, T. S. & Camilo, F. F. Free facile Preparation of Ag-nanoparticles on cellulose membrane for catalysis. *Cellulose* **28**, 4899–4911 (2021).
48. Noguez, C. Surface plasmons on metal nanoparticles: the influence of shape and physical environment. *J. Phys. Chem. C.* **111**, 3806–3819 (2007).
49. Mulvaney, P. Surface plasmon spectroscopy of nanosized metal particles. *Langmuir* **12**, 788–800 (1996).
50. Treguer, M. et al. Dose rate effects on radiolytic synthesis of Gold – Silver bimetallic clusters in solution. *J. Phys. Chem. B.* **102**, 4310–4321 (1998).
51. Garcia, M. A. Surface plasmons in metallic nanoparticles: fundamentals and applications. *J. Phys. D: Appl. Phys.* **44**, 283001 (2011).
52. Mostafavi, M., Delcourt, M. O., Keghouche, N. & Picq, G. Early steps of formation of silver/polyacrylate complexed oligomer clusters. A pulse radiolysis study. *Int. J. Radiat. Appl. Instrum. Part. C Radiat. Phys.* **40**, 445–450 (1992).
53. Hwang, I. T. et al. Green and efficient radiation-based Preparation of crosslinked poly(vinyl pyrrolidone)-iodine (PVP-I)-introduced polypropylene (PP) sheets for antibacterial wound dressing application. *Eur. Polym. J.* **208**, 112848 (2024).
54. Shumi, G. et al. Biosynthesis of silver nanoparticles functionalized with histidine and phenylalanine amino acids for potential antioxidant and antibacterial activities. *ACS Omega.* **8**, 24371–24386 (2023).
55. Nandiyanto, A. B. D., Oktiani, R. & Ragadhita, R. How to read and interpret FTIR spectroscope of organic material. *Indonesian J. Sci. Technol.* **4**, 97 (2019).
56. Zeariya, M. G. M. et al. Improvement of antibacterial activity of AgNPs@PVA-PVP ternary nanocomposite films followed by gamma-ray irradiation treatment for biomedical applications. *Radiat. Phys. Chem.* **226**, 112345 (2025).
57. Lee, I. et al. One-pot gamma ray-induced green synthesis of a Prussian blue-laden polyvinylpyrrolidone/reduced graphene oxide aerogel for the removal of hazardous pollutants. *J. Mater. Chem. A.* **7**, 1737–1748 (2019).
58. Velgosova, O., Mudra, E. & Vojtko, M. Preparing, characterization and Anti-Biofilm activity of polymer fibers doped by green synthesized AgNPs. *Polymers* **13**, 605 (2021).
59. Kim, N. Y., Leem, Y. C., Hong, S. H., Park, J. H. & Yim, S. Y. Ultrasensitive and stable plasmonic Surface-Enhanced Raman scattering substrates covered with atomically thin monolayers: effect of the insulating property. *ACS Appl. Mater. Interfaces.* **11**, 6363–6373 (2019).
60. Ferraria, A. M. & Carapeto, A. P. Botelho do Rego, A. M. X-ray photoelectron spectroscopy: silver salts revisited. *Vacuum* **86**, 1988–1991 (2012).
61. Wang, K. et al. Multifunctional silk fibroin/PVA bio-nanocomposite films containing TEMPO-oxidized bacterial cellulose nanofibers and silver nanoparticles. *Cellulose* **29**, 1647–1666 (2022).
62. Maiti, N., Thomas, S., Debnath, A. & Kapoor, S. Raman and XPS study on the interaction of taurine with silver nanoparticles. *RSC Adv.* **6**, 56406–56411 (2016).
63. Wu, Y. et al. The shape evolution of gold seeds and gold@silver core–shell nanostructures. *Nanotechnology* **20**, 305602 (2009).

64. Malvankar, S. et al. Co-Doped SnO2 nanocrystals: XPS, Raman, and magnetic studies. *J. Electron. Mater.* **49**, 1872–1880 (2020).
65. Vinita et al. Nanonetwork of coordination polymer AHMT-Ag for the effective and broad spectrum detection of 6-Mercaptopurine in urine and blood serum. *ACS Omega.* **4**, 16733–16742 (2019).
66. Korshed, P., Li, L., Ngo, D. T. & Wang, T. Effect of storage conditions on the Long-Term stability of bactericidal effects for laser generated silver nanoparticles. *Nanomaterials* **8**, 218 (2018).
67. Phan, H. T. & Haes, A. J. What does nanoparticle stability mean? *J. Phys. Chem. C.* **123**, 16495–16507 (2019).
68. Salimiyan Rizi, K. MXene nanosheets as a novel nanomaterial with antimicrobial applications: A literature review. *J. Mol. Struct.* **1262**, 132958 (2022).
69. Durán, N. et al. Silver nanoparticles: A new view on mechanistic aspects on antimicrobial activity. *Nanomed. Nanotechnol. Biol. Med.* **12**, 789–799 (2016).
70. Premanathan, M., Karthikeyan, K., Jeyasubramanian, K. & Manivannan, G. Selective toxicity of ZnO nanoparticles toward Gram-positive bacteria and cancer cells by apoptosis through lipid peroxidation. *Nanomedicine* **7**, 184–192 (2011).
71. Acharya, D. et al. Shape dependent physical mutilation and lethal effects of silver nanoparticles on bacteria. *Sci. Rep.* **8**, 201 (2018).
72. Ferreyra Maillard, A. P. V. et al. Studies on interaction of green silver nanoparticles with whole bacteria by surface characterization techniques. *Biochim. Biophys. Acta Biomembr.* **1861**, 1086–1092 (2019).
73. Wang, Z. X. et al. Ångstrom-Scale silver particles as a promising agent for Low-Toxicity Broad-Spectrum potent anticancer therapy. *Adv. Funct. Mater.* **29**, 1808556 (2019).
74. Hsiao, I. L., Hsieh, Y. K., Wang, C. F., Chen, I. C. & Huang, Y. J. Trojan-Horse mechanism in the cellular uptake of silver nanoparticles verified by direct Intra- and extracellular silver speciation analysis. *Environ. Sci. Technol.* **49**, 3813–3821 (2015).
75. Li, T, et al. Bacterial resistance to antibacterial agents: Mechanisms, control strategies, and implications for global health. *Sci. Total Environ.* **860**, 160461 (2023).
76. Menichetti, A., Mavridi-Printezi, A., Mordini, D. & Montalti, M. Effect of Size, shape and surface functionalization on the antibacterial activity of silver nanoparticles. *J. Funct. Biomater.* **14**, 244 (2023).
77. Song, J. et al. Multifunctional antimicrobial biometallohydrogels based on amino acid coordinated Self-Assembly. *Small* **16**, 1907309 (2020).
78. Feng, Q. L. et al. A mechanistic study of the antibacterial effect of silver ions on Escherichia coli and Staphylococcus aureus. *J. Biomed. Mater. Res.* **52**, 662–668 (2000).
79. Casals, E., Gusta, M. F., Bastus, N., Rello, J. & Puntes, V. Silver nanoparticles and antibiotics: A promising synergistic approach to Multidrug-Resistant infections. *Microorganisms* **13**, 952 (2025).

Acknowledgements

Author contributions

W.L., H.R., D.F. and R.G. conceived the experiments. W.L. conducted the experiments and performed statistical analysis and figure generation. D.D. performed the XPS studies and analyzed the data. All authors reviewed the manuscript.

Declarations

Competing interests

The authors declare no competing interests.

Additional information

Supplementary Information The online version contains supplementary material available at https://doi.org/10.1038/s41598-025-24235-w.

Correspondence and requests for materials should be addressed to D.F., H.R. or R.G.

Reprints and permissions information is available at www.nature.com/reprints.

Publisher's note Springer Nature remains neutral with regard to jurisdictional claims in published maps and institutional affiliations.